



LAWRENCE
LIVERMORE
NATIONAL
LABORATORY

LLNL-JRNL-512873

Edge-localized mode control and transport generated by externally applied magnetic perturbations

I. Joseph

November 10, 2011

Contributions to Plasma Physics

Disclaimer

This document was prepared as an account of work sponsored by an agency of the United States government. Neither the United States government nor Lawrence Livermore National Security, LLC, nor any of their employees makes any warranty, expressed or implied, or assumes any legal liability or responsibility for the accuracy, completeness, or usefulness of any information, apparatus, product, or process disclosed, or represents that its use would not infringe privately owned rights. Reference herein to any specific commercial product, process, or service by trade name, trademark, manufacturer, or otherwise does not necessarily constitute or imply its endorsement, recommendation, or favoring by the United States government or Lawrence Livermore National Security, LLC. The views and opinions of authors expressed herein do not necessarily state or reflect those of the United States government or Lawrence Livermore National Security, LLC, and shall not be used for advertising or product endorsement purposes.

Edge-localized mode control and transport generated by externally applied magnetic perturbations

Ilon Joseph^{*1}

¹ Lawrence Livermore National Laboratory, P. O. Box 808, Livermore CA 94551, USA

Received XX November 2011, revised XX November 2011, accepted XX December 2011

Published online XX December 2011

Key words tokamak, edge localized mode control, magnetic perturbations, quasilinear transport

PACS 04A25

This article reviews the subject of edge localized mode (ELM) control using externally applied magnetic perturbations and proposes theoretical mechanisms that may be responsible for the induced transport changes. The first question that must be addressed is: what is the structure of magnetic field within the plasma? Although initial hypotheses focused on the possibility of the creation of a region of stochastic field lines at the tokamak edge, drift magnetohydrodynamics theory predicts that magnetic reconnection is strongly suppressed over the region of the pedestal with steep gradients and fast perpendicular rotation. Reconnection can only occur near the location where the perpendicular electron velocity vanishes, and hence the electron impedance nearly vanishes, or near the foot of the pedestal, where the plasma is sufficiently cold and resistive. The next question that must be addressed is: which processes are responsible for the observed transport changes, nonlinearity, turbulence, or stochasticity? Over the pedestal region where ions and electrons rotate in opposite directions relative to the perturbation, the quasilinear Lorentz force decelerates the electron fluid and accelerates the ion fluid. The quasilinear magnetic flutter flux is proportional to the force and produces an outward convective transport that becomes significant if the resistive layer width becomes smaller than the ion gyroradius. Over the pedestal region where the $E \times B$ flow and the electrons rotate in opposite directions relative to the perturbation, magnetic islands with a width on the order of the ion gyroradius can directly radiate drift waves. If flux surfaces are broken, the combination of stochastic electron transport and ion viscous transport can lead to a large net particle flux. Since there are many transport mechanisms that may be active simultaneously, it is important to determine which physical mechanisms are responsible for ELM control and to predict the scaling to future devices.

Copyright line will be provided by the publisher

1 Introduction

Next-generation tokamak fusion reactors need techniques to reduce the heat exhaust to a level that is acceptable for the lifetime of plasma facing divertor components. Transient events, such as edge localized modes (ELMs) [1], which are associated with high-confinement mode (H-mode), must limit the heat impulse that is delivered. Extrapolations of ELM sizes from present devices to ITER predict 10-20 MW/event given estimates for the pedestal height [2], yet tolerable ELM heat impulses must be limited to less than 1 MW/event [3] or, perhaps, even less. Such predictions for type-I ELM sizes imply that it will be necessary to either suppress type-I ELMs or mitigate their heat fluxes in order to maintain an acceptable divertor lifetime [4]. It is important to note that, while ELMs limit the confinement time by generating edge transport, ELMs also play the beneficial role of flushing impurities from the edge plasma. So-called ELM-free H-mode operating regimes have difficulty controlling plasma density, lead to an undesirable build-up of high-Z impurities, and lead to a back-transition to L-mode [1]. Any technique for controlling ELMs must also generate enough transport to maintain density control and keep impurities from poisoning the core. Hence, rather than completely suppress ELMs, it may be desirable to generate or actively trigger smaller edge instabilities at a pace that is consistent with tolerable erosion and transport requirements.

* Corresponding author: e-mail: joseph5@llnl.gov, Phone: +01 925 422 3737, Fax: +01 925 423 3484

This article reviews present theoretical understanding of ELM control using externally generated non-axisymmetric magnetic perturbations. This technique can be used to eliminate ELMs entirely (suppression) [5, 6, 7, 8], to continuously generate more benign edge instabilities (mitigation) [9, 10], or to actively trigger smaller-scale ELMs at a more rapid pace (triggering) [11, 12, 13]. Thus, updated ITER designs have considered external coils that generate such perturbations [14, 15]. The next section presents a brief overview of the presently known experimental ELM control regimes that are induced by non-axisymmetric magnetic perturbations. The recent review by Liang [16] addresses the experimental status of ELM control using non-axisymmetric magnetic perturbations as well as a number of other control techniques such as ELM pacing through fuel pellet injection or through axisymmetric vertical jogs of the plasma surface. Operation in a specific regime where type-I ELMs are passively stabilized and another instability dominates transport is another important route for ELM mitigation. The review by Oyama [17] discusses a number of such regimes including QH-mode, type-III ELMs, and type-V ELMs. New regimes such as I-mode [18] may still await discovery.

The physics of non-axisymmetric perturbations is complex and few issues have been solved completely, particularly at the plasma edge where there are strong gradients (e.g. the pedestal), kinetic/neoclassical effects (e.g. large trapped particle fraction at low collisionality) and changes in geometry and sources (e.g. separatrix and neutrals). The general single-fluid magnetohydrodynamics (MHD) equations for the case of closed surfaces with thin island layers has recently been reviewed by Boozer [19], where the relation between non-ambipolar transport due to non-axisymmetric fields and plasma torque is explained. A comprehensive set of multi-fluid transport relations has recently been derived by Callen [20]. In the pedestal, it is important to retain drift effects when treating so-called “resonant” magnetic perturbations, perturbations with a helicity that resonates with field lines; i.e. $k_{\parallel} \propto m - qn = 0$ where m is the poloidal harmonic, n is the toroidal harmonic, q is the safety factor, and R is the major radius. The reason is that (i) the diamagnetic frequencies are typically larger than the $E \times B$ frequency and (ii) the collisionality is typically low enough that the characteristic resistive scale length is smaller than the ion gyroradius. If the response layer is of the order of the ion gyroradius, then a kinetic description will be necessary. For simplicity, here, two-fluid drift-MHD equations are considered in order to display the general linear response to resonant magnetic perturbations. Finally, it is useful to consider the effect of (iii) anomalous/viscous transport, which is faster than the time scale for resistive diffusion.

The original hypothesis put forward to explain the ability of non-axisymmetric magnetic fields to control ELMs was that the magnetic field at the edge of the plasma would become stochastic [9, 21] and the criterion for achieving stochasticity is commonly used as figure of merit for the design of perturbation coils. However, magnetic reconnection is strongly suppressed in a plasma that rotates in the perpendicular direction [22] and strong perpendicular diamagnetic rotation is a basic requirement of magnetic confinement at the edge of the H-mode pedestal. Measured changes to transport are either slight or are observed to have a large impact on particle transport, not thermal transport. In fact, certain ELM control experiments routinely observe an increase in the electron temperature gradient in the pedestal region, rather than a decrease, as would be expected in a stochastic magnetic field [23] and as has been measured in previous ergodic divertor studies in L-mode [24]. Thus, the supposition that an ergodic divertor would develop and limit the pedestal pressure gradient by controlling the edge electron temperature [25] appears inconsistent with the data. A number of theoretical estimates and calculations [7, 26, 27, 28, 29] have shown that pedestal transport changes cannot be explained by this hypothesis. Calculations for the magnetic field structure show significant modifications by the response of the plasma to the applied fields [30, 31, 32, 33, 34, 35].

In this article, physical mechanisms that are capable of explaining changes to particle transport are qualitatively considered. An overview of the present experimental results is given in Sec. 2 and the description of the plasma equilibrium and particle fluxes are defined in Sec. 3. Any transport mechanism that increases the effective diffusivity with a δD that depends on the ratio of the magnetic perturbation field to the background field $\delta B/B$ must exceed the background transport level with diffusivity D_0 in order to be observed. The requirement $\delta D > D_0$ sets a threshold for $\delta B/B$ that depends on plasma parameters such as collisionality and shaping that depend on the transport mechanisms that determine the diffusivities. The structure of the magnetic perturbation inside the plasma is the first question that must be addressed. Section 4 discusses the linear ideal and non-ideal plasma response to an external perturbation. The plasma will resist reconnection by attempting to shield the resonant helicity components of the perturbation. At the same time, the plasma can strongly amplify neighboring helicities if the perturbation couples well to an internal mode. The nature of the transport mechanism is the next

question that must be addressed. Section 5 considers steady-state transport changes caused by the nonlinear perturbation structure: quasilinear, neoclassical, and stochastic transport. The transport generated by small islands or a stochastic field is used to estimate the induced ambipolar $E \times B$ flux [35]. The axisymmetric poloidal neoclassical viscous force will allow relatively large ambipolar transport if quasilinear forces are taken into consideration [29, 36, 37, 38]. Section 6 considers possible changes to turbulent transport. Damping of the toroidal rotation profile or of zonal flows may be large enough to affect turbulent transport. In addition, sufficiently small islands, on the order of the ion gyroradius in width, can directly radiate drift waves. The final section concludes with a summary of results.

2 Experimental overview

At present, ELM control using non-axisymmetric magnetic perturbations appears to manifest in a number of separate regimes depending on experimental configuration and tokamak facility. First, Sec. 2.1 describes three of the observed regimes based on differences between collisionality and geometry: (i) high-collisionality ELM mitigation, (ii) low-collisionality ELM suppression and (iii) ELM pacing. Next, Sec. 2.2 discusses the relevance of using the Chirikov criterion for magnetic stochasticity, which has been advocated as an experimental figure of merit [21]. Finally, Sec. 2.3 examines a typical low-collisionality ELM-suppressed discharge. It will be seen that extensions of ideal MHD are necessary for an accurate description of the pedestal region. The key conclusions are: (i) the $E \times B$ velocity is smaller than the diamagnetic velocities and, in fact, the ions and electron rotate in opposite directions at the edge; (ii) the resistive scale is smaller than the ion Larmor radius, which implies that finite Larmor radius (FLR) effects are important; and (iii) anomalous diffusivity and viscosity are much larger than the resistive diffusion of magnetic flux, which implies that it is important to include anomalous transport.

2.1 Observed ELM control regimes

(i) *High-collisionality ELM mitigation*, the first regime found on DIII-D [9, 5, 39, 40], observed the replacement of large type-I ELMs by much smaller transient events. The toroidal mode number $n = 3$ perturbations had little effect on the plasma profiles, but were found to strongly damp toroidal rotation. ASDEX-Upgrade has recently discovered an ELM control regime that shares certain similarities [10]. For ASDEX-Upgrade, there is a clear threshold in either collisionality or density that must be exceeded in order for type-I ELMs to disappear. During mitigation, there is an enhancement in plasma density n_e , and presumably particle confinement. Both ASDEX-Upgrade and DIII-D found that the perturbation strength must exceed a threshold in perturbation amplitude on the last closed flux surface of roughly $\delta B/B > 10^{-3}$, but the results are not very sensitive to the mode spectrum. The edge pressure gradient does not change appreciably and should still be unstable to type-I ELMs according to ideal peeling-balloon theory [41, 42]. The nonlinear effect of such a perturbations on the evolution of a type-I ELMs is anticipated to be relatively small; thus, it might be suspected that a new, non-ideal edge instability has become unstable enough to dominate transport. On DIII-D, non-axisymmetric striation of the strike-points was observed and explained as the bifurcation of the poloidal separatrix into a “homoclinic tangle” [43]. However, further investigation showed that the structure appeared to be more consistent with the formation of an amplified $n = 1$ mode that may have also been responsible for damping rotation [44].

(ii) *Low-collisionality ELM suppression* was discovered on DIII-D [5, 6, 7] soon after the high-collisionality cases described above. When an $n = 3$ perturbation is activated during H-mode, there is a prompt change in turbulent fluctuations [45] and fluxes at the target plate [46]. An initial transient phase, on the order of the transport time scale, typically ensues where ELMs become smaller and more frequent before being completely eliminated. During this phase, the plasma density is reduced due to an increase in particle transport and, in β -feedback mode, the temperatures increase, maintaining the H-factor. This technique can also generate smaller, more frequent ELMs on JET using $n = 2$ fields [47] and on MAST using $n = 3$ fields [48], although complete suppression has not been observed. The results have similar phenomenology in that they require (i) the resonant harmonic of the perturbation amplitude to exceed a given threshold, roughly $\delta B_{m=qn}/B > 10^{-4}$, (ii) the collisionality to be lower than a given threshold, e.g. $\nu_* < 0.5$ for MAST, and (iii) the edge q_{95} to be in a narrow window, typically of order $\Delta q_{95} \sim 0.1$. ELM suppression appears to occur by reducing the edge pressure gradient and thus bootstrap current drives for peeling-balloon modes [6, 49]. However, since the edge density pedestal is reduced and the steep part of the edge electron temperature gradient is observed to increase, the maximum pressure gradient is

not necessarily reduced. The electron temperature at the top of the pedestal flattens and reduces the width of the peak gradient region and the overall effect is to reduce the global drive for instability. The strike point develops multiple helical striations in particle flux [26, 50]; however, the heat flux deposition pattern remains essentially axisymmetric [50, 51] which signals a very shallow penetration of the tangle into the pedestal. ELMs remaining during the incomplete suppression phase, which do penetrate into the pedestal, generate heat flux patterns that are close to expectations of the tangle structure based on the applied perturbation fields [51].

(iii) *ELM pacing* has been used to control impurities in Lithium coated discharges on NSTX [12, 13]. Lithium coating of the divertor target plates represents another route to ELM suppression; however, like ELM-free H-mode, impurities tend to collect in the core and eventually degrade performance. ELM pacing using magnetic perturbations leads to a desirable operating scenario where impurities are controlled. In some cases, it can be shown that the edge temperature gradient increases sufficiently to cause destabilization of an ELM. In order to control density during ELM-free H-mode, JFT-2M has also used magnetic perturbations to achieve a continuous destabilization of ELMs [11]. In general, large perturbations can cause a back-transition to L-mode that is qualitatively similar to an ELM event as reported for MAST in [48, 52, 53]. For NSTX, significant divertor heat and particle flux striations occur that are well matched to predicted connection length profiles [54, 55]. These predictions can arbitrarily set the depth that field lines penetrate into the pedestal by treating the plasma as ideal within a certain control surface and as a vacuum outside of this surface. However, the connection length profiles are found to be relatively insensitive to the location of the ideal-stochastic control surface.

2.2 The Chirikov criterion for magnetic stochasticity

Much theoretical attention has addressed low collisionality ELM suppression, case (ii), and less attention has focused on the other two cases. Both suppression and triggering require the pitch-resonant Fourier harmonics of the normal field perturbation to exceed a threshold. The requirement of pitch-resonance motivated the study of the formation of magnetic islands or stochastic regions. A magnetic perturbation δB_{mn} that is resonant at a rational surface r_s , given implicitly by $q(r_s) = m/n$ where m is the poloidal and n is the toroidal harmonic, generates a magnetic island of (full) width

$$w = 4 \sqrt{\left| \frac{Rr_s}{ns} \frac{\delta B_{m=qn}}{B} \right|} \quad (1)$$

where the global magnetic shear is defined by $s = d \log q / d \log r$. (For an expression that is accurate in toroidal geometry, see [27]). Since the spacing between rational surfaces of a given toroidal harmonic is $\delta r_s = 1/nq' = r_s/nqs$, islands will overlap and generate a stochastic layer once the Chirikov parameter

$$\sigma = \frac{w}{\delta r_s} = 4 \sqrt{\left| \frac{sq^2 R}{r_s} \frac{\delta B_{m=qn}}{B} \right|} \quad (2)$$

becomes larger than unity. In fact, a correlation between ELM suppression and the Chirikov parameter was found in Ref. [21]. Such studies typically assume that the magnetic perturbations in the plasma are the same as the fields produced with no plasma at all, the so-called “vacuum approximation.” However, at fixed q , the Chirikov criterion is really a combined measure of $\delta B/B$ and of the edge shear $s = d \log q / d \log r$. Due to the small window of Δq_{95} where ELM suppression actually occurs, it is difficult to independently determine the dependence on shear. In fact, because the fields within the plasma have not been measured to date, it is only the threshold in the vacuum field $\delta B_{vac}/B$ that is actually well-determined.

The stochasticity interpretation met with immediate difficulties since: (i) The observed transport effects appear to contradict analytic estimates and numerical calculations. (ii) There is a very small window in edge q_{95} where suppression is found, rather than the $\mathcal{O}(1)$ region of Δq_{95} where island overlap would occur in the vacuum approximation. (iii) There are measured dependences on dimensionless parameters such as shaping, collisionality, and plasma $\beta = 2\mu_0 p / B^2$, but the predictions of stochasticity are relatively insensitive to these parameters. (iv) Finally, the high-collisionality ELM mitigation experiments do not appear to be sensitive to the pitch-resonance of the spectrum.

One of the most robust effects appears to be a change in particle transport. When experiments are run at fixed global pressure (β -feedback), the temperature tends to change a manner that somewhat compensates for the

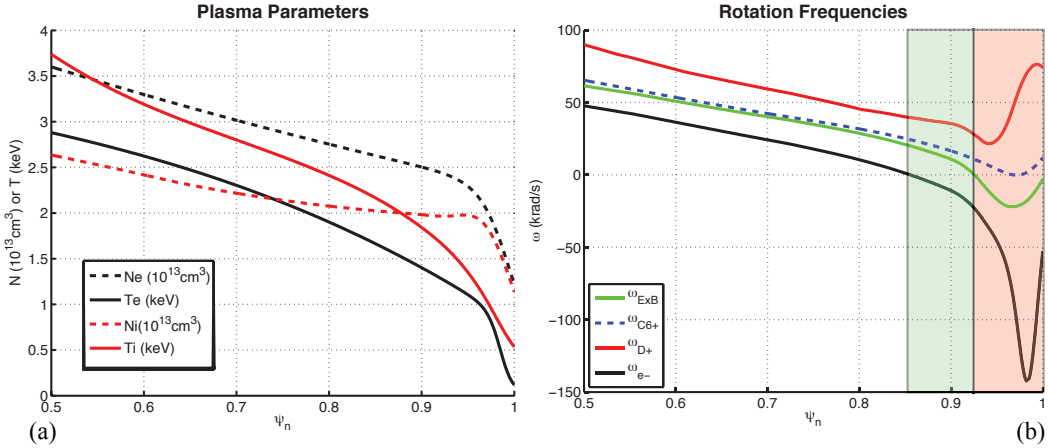


Fig. 1 Plasma parameters vs. normalized poloidal flux ψ_n for the low-collisionality ELM suppressed DIII-D discharge 126006. (a) Electron and deuterium ion density $n_{e,i}$ and temperature $T_{e,i}$. (b) The perpendicular (toroidal) rotation frequency (Eq. ??) profiles measured for the CVI+ impurity species (blue dashed) and inferred from radial force balance (Eq. 8): $E \times B$ (green), deuterium (red), and electron (black) frequencies. The $E \times B$ flow and the electrons rotate in opposite directions ($\omega_e \omega_e < 0$) over the green shaded region $0.85 < \psi_n < 0.925$. The ions and electrons rotate in opposite directions ($\omega_e \omega_i < 0$) over the entire red and green shaded region $0.85 < \psi_n$.

change in plasma density: when density is reduced, temperatures increase, and vice-versa. This is not consistent with stochastic electron thermal transport, even when fairly sophisticated models are used, unless the magnetic field perturbations are strongly suppressed near the separatrix [26, 27, 29, 37]. The transport models are consistent with an isolated island or stochastic region that develops at the top of the pedestal, e.g. see [29]. However, it is important to consider other types of transport mechanisms as well.

2.3 Example of a low-collisionality ELM-suppressed pedestal

Plasma parameters for the ELM-suppressed DIII-D discharge #126006, which has been well-studied [29, 30, 31, 32], are shown in Fig. 1(a) over the outer 50% of the normalized poloidal flux ψ_n . In the ELM-suppressed phase, the density drops by roughly a factor of 2 at the edge, while the temperatures somewhat increase. The curves are fits to data that is mapped to inferred location on equilibrium flux surfaces and were prepared using the pedestal analysis of Ref. [49]. The electron density n_e (black solid) and temperature T_e (black dashed) are measured via Thomson scattering while the carbon ion impurity (CVI+) density, temperature T_i (red dashed), and velocity are measured via charge exchange recombination spectroscopy (CER) and used to determine the ion density n_i (red solid).

Perpendicular (toroidal) rotation frequencies are shown in Fig. 1(b) with a normalization convention described in Eq. 11 of Sec. 3.2. Charge exchange recombination spectroscopy is used to directly measure the carbon impurity ion perpendicular rotation profile (CIV+ dashed blue). Radial force balance (Eq. 8) is then used to infer the perpendicular rotation of the $E \times B$ frame Ω_E (green), deuterium Ω_i (red), and electrons Ω_e (black), from the diamagnetic rotation profiles due to the pressure profiles in Fig. 1(a). It is clear that $E \times B$ rotation frequency is smaller than the diamagnetic rotation frequency in the steep gradient region of the pedestal. It is important to emphasize that, since the electron temperature gradient is much steeper than the ion temperature gradient, the electrons and ions can rotate in opposite directions at the edge of the pedestal for $\psi_n > 0.85$ (the shaded region shown in green in Fig. 1(b)). (Note that these profiles were not available to Ref. [30], and the assumptions used there modified the location of the electron null point to $\psi_n \simeq 0.6$).

Figure 2(a) demonstrates that the low collisionality produces an extreme range of time scales. The Alfvén time scale $\tau_A = R/V_A$ (black dashed) and hydromagnetic time scale $\tau_H = \tau_A/sn$ (black solid) are of order $10^{-8} - 10^{-7} \text{ s}$. The energy confinement time scale inferred by estimating the ion thermal diffusivity χ_i from the ion temperature profile $\tau_{Ti} = r^2/\chi_i$ (blue solid) varies from $10^{-2} - 1 \text{ s}$ (compare to the curve τ_{1m^2s} for a diffusivity of $1 \text{ m}^2/\text{s}$ (dashed blue)) and is much shorter than the resistive time scale $\tau_R = r^2\mu_0/\eta_{||}$ (red dashed)

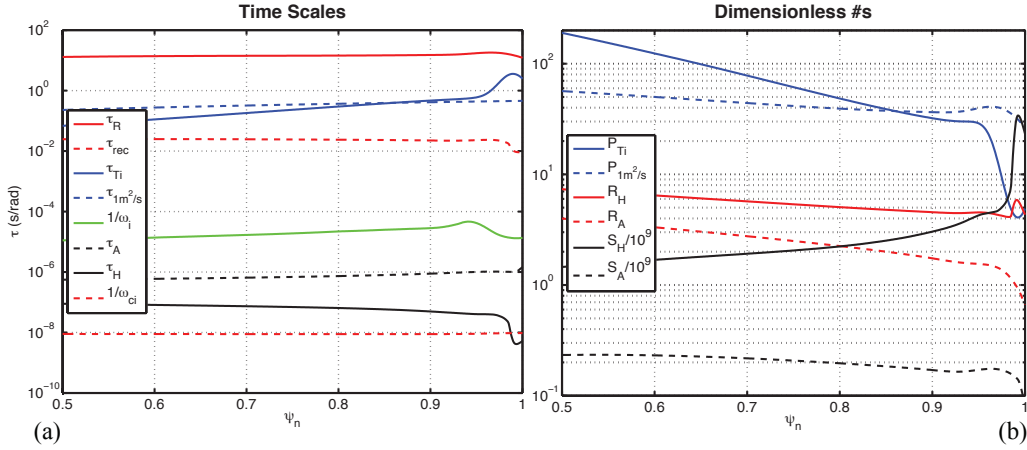


Fig. 2 Analysis of times scales corresponding to Fig. 1. (a) Time-scales: inverse ion cyclotron frequency $1/\omega_{ci}$, hydromagnetic time $\tau_H = qR/nsV_A$, Alfvén time $\tau_A = qR/nV_A$, inverse ion rotation frequency $1/\omega_i$, resistive time scale $\tau_R = r^2\mu_0/\eta_{||}$, and visco-resistive time scale $\tau_{rec} = S_H^{1/3}\tau_R$. (b) Dimensionless constants: Lundquist #'s $S_A = \tau_A/\tau_R$, $S_H = \tau_H/\tau_R$; “Prandtl” #'s $P_{Ti} = \tau_{Ti}/\tau_H$, $P_{1m^2/s} = \tau_R/\tau_{1m^2/s}$, and FLR parameter $R_H = \rho_{cs}/\delta_{rec,H}$ the ratio of the ion sound gyroradius to resistive layer width $\delta_{rec,H} = S_H^{-1/3}r$.

which is on the order of 10 s. Figure 2(b) shows that the Lundquist number $S_A = \tau_R/\tau_A$ (black dashed) and the hydromagnetic Lundquist numbers $S_H = \tau_H/\tau_R$ (black solid) are as large as $10^8 - 10^9$. This allows one to estimate that the basic resistive reconnection time scale $\tau_{rec} = S_H^{-2/3}\tau_H$ (red dashed) is on the order of 10-100 ms. The ion rotation frequency $\omega_i = \omega_E - \omega_{*i}$ is much faster than τ_{rec} , which implies that reconnection is strongly suppressed in the single-fluid MHD model [22]. The characteristic resistive length scale $\rho_{rec} = S_H^{-1/3}r$ is smaller than the ion gyroradius, which implies that FLR effects can play an important role.

3 Definitions of particle transport and equilibrium

In a magnetized plasma, the particle flows are determined from a drift expansion of the fluid equations (Sec. 3.1). The assumption of radial force balance requires a toroidal equilibrium magnetic field geometry and determines the drift flows within a magnetic surface. Section 3.2 describes the geometric conventions (co- and contra-variant indices) used in this article and presents three equivalent expressions for the net radial current. Finally, Sec. 3.3 discusses the constraint of ambipolarity: any perpendicular current must generate a parallel return current.

3.1 Fluid equations

Particle and momentum balance for each charged particle species is given by the fluid equations

$$\partial_t n + \nabla \cdot n \mathbf{V} = 0 \quad (3)$$

$$\partial_t mn \mathbf{V} + \nabla \cdot (mn \mathbf{V} \mathbf{V} + p + \boldsymbol{\pi}) = Zen(\mathbf{E} + \mathbf{V} \times \mathbf{B}) + \mathbf{R}. \quad (4)$$

with mass m , electron charge e , charge state Z , density n , velocity \mathbf{V} , pressure p , viscous tensor $\boldsymbol{\pi}$, and the friction force \mathbf{R} . The first two fluid moments determine the evolution of the system if a closure for the pressure and viscous tensor $\boldsymbol{\pi}$ is specified. For a magnetized plasma, the gyrofrequency $\omega_c = ZeB/m$ and gyroradius $\rho_c = V_T/\omega_c$, where $V_T = \sqrt{T/m}$ is the thermal velocity, set the fundamental scales. The drift expansion employs the small parameter $\delta \sim \omega/\omega_c \sim \nu/\omega_c$, where ω is a characteristic dynamical frequency and ν is a characteristic collisional frequency. Near a rational surface, microscopic scales that are smaller than the ion gyroradius can be generated; however, in order to simplify the discussion, it is assumed that the smallest spatial scales of interest w satisfy the ordering $\rho_c/w \sim \mathcal{O}(\delta)$. Given this ordering, force balance Eq. 4 yields an

expression for the flow accurate to order δ^2 :

$$\mathbf{V} = V_{\parallel} \mathbf{b} + \frac{\mathbf{b} \times \mathbf{E}}{B} + \frac{\mathbf{b} \times \nabla p}{ZenB} + \left(\frac{\mathbf{b} \times (\frac{d}{dt} mn \mathbf{V} + \nabla \cdot \boldsymbol{\pi} - \mathbf{R})}{ZenB} \right) + \dots \quad (5)$$

3.2 Equilibrium fields, flows, and geometry

The solution is expanded order by order in δ via $\mathbf{B} = \mathbf{B}_0 + \delta \mathbf{B}_1 + \dots$. Since the perturbations of interest are rather small $\delta B/B_0 \sim 10^{-4} - 10^{-3}$, they are assumed to arise at order $\delta \mathbf{B}_1$. Thus, MHD force balance $\mathbf{J}_0 \times \mathbf{B}_0 = \nabla p_0$ must hold to lowest order, given the assumption of quasineutrality. This implies that the equilibrium magnetic field \mathbf{B}_0 can be assumed to have toroidal magnetic surfaces due to the constraint $\mathbf{B}_0 \cdot \nabla p_0(r) = 0$, where r is a generalized radial coordinate parameterizing the surfaces (assuming that $B_0 \neq 0$ and $p'_0 \neq 0$.) In magnetic coordinates with poloidal angle θ and toroidal angle ζ , this implies that the magnetic field has the representation

$$\mathbf{B}_0 = \nabla \psi_\theta(r) \times \nabla \theta + \nabla \zeta \times \nabla \psi_\zeta(r) = B^\theta (\partial_\theta \mathbf{x} + q(r) \partial_\zeta \mathbf{x}). \quad (6)$$

The convention for vector indices used in this article is that $B^\theta \equiv \mathbf{B}_0 \cdot \nabla \theta$ is a contravariant component and $B_\theta = \mathbf{B}_0 \cdot \partial_\theta \mathbf{x}$ is a covariant component. The safety factor $q(r) \equiv d\psi_\theta/d\psi_\zeta$ yields the field line equations $d\zeta/d\theta = q$ along unperturbed field lines. The definitions imply that $B^\zeta = qB^\theta = \psi'_\theta/\mathcal{J}$ where $X' = dX/dr$ and the Jacobian is $\mathcal{J} = \partial_r \mathbf{x} \cdot \partial_\theta \mathbf{x} \times \partial_\zeta \mathbf{x}$. The relatively large parallel thermal and electric conductivities imply that the equilibrium temperature $T_0(r)$, electron density $n_0(r)$, and potential $\phi_0(r)$ are all flux functions to lowest order.

The Lorentz force acting on each species (labeled by subscript j) determines the lowest order perpendicular flow via $\mathbf{f}_j \equiv Z_j e n_j \mathbf{V}_j \times \mathbf{B}$. Radial force balance yields the drift frequency

$$\Omega_j \equiv V_j^\zeta - qV_j^\theta = f_{jr}/Z_j e n_j \psi'_\zeta \quad (7)$$

and, to lowest order in δ , the equilibrium drift frequency is

$$\Omega_{j,0} = -\phi'_0/\psi'_\zeta - p'_{j,0}/Z_j e n_{j,0} \psi'_\zeta. \quad (8)$$

Parallel force balance implies that the total force must be perpendicular $\mathbf{B} \cdot \mathbf{f}_j = 0$ and thus, $f_{j\theta}/f_{j\zeta} = -B^\zeta/B^\theta = -q$. This leads to three equivalent forms for the radial current of species j

$$Z_j e \Gamma_j^r = Z_j e n V_j^r = (f_{j\zeta} B_\theta - f_{j\theta} B_\zeta)/\mathcal{J} B^2 = f_{j\zeta}/\psi'_\zeta = -f_{j\theta}/\psi'_\theta. \quad (9)$$

In this article, we adopt the commonly used convention of expressing the drift frequency as an equivalent toroidal frequency $\Omega \equiv V^\zeta - qV^\theta$, e.g. as defined in Eq. 7. In general, for a mode with wavenumber $\mathbf{k} = -m\nabla\theta + n\nabla\zeta$, the Doppler frequency is $\omega_V = \mathbf{k} \cdot \mathbf{V} = nV^\zeta - mV^\theta$ and the parallel Doppler frequency is

$$\omega_{V,\parallel} = k_{\parallel} V_{\parallel} = (nq - m)(V^\zeta B_{tor}^2 + qV^\theta B_{pol}^2)/qB^2. \quad (10)$$

The perpendicular Doppler frequency is proportional to the drift frequency Ω :

$$\omega_{V,\perp} = \mathbf{k}_{\perp} \cdot \mathbf{V}_{\perp} = (V^\zeta - qV^\theta)(mB_{tor}^2 + qnB_{pol}^2)/qB^2. \quad (11)$$

and is typically of order $m\Omega/q$. For a resonant mode that satisfies $m = qn$, the parallel Doppler frequency vanishes and the perpendicular Doppler frequency is precisely $n\Omega$.

3.3 The constraint of ambipolarity

Quasineutrality is described by the condition of current continuity: $\nabla \cdot \mathbf{J} = \nabla \cdot J_{\parallel} \mathbf{b} + \nabla \cdot \mathbf{J}_{\perp} = 0$, which requires parallel and perpendicular current flows to balance. For each species, the individual components of the particle flux can be written as the sum $\Gamma = \Gamma_V + \Gamma_E + \Gamma_p + \Gamma_{pol} + \Gamma_{\pi} + \Gamma_R + \dots$, corresponding to the consecutive

terms in Eq. 5. The net flux advected through any topologically toroidal surface r is defined through the surface average

$$\langle \Gamma^r \rangle = \int \Gamma^r \mathcal{J} d\theta d\zeta / \mathcal{A} \quad (12)$$

where the flux surface area is $\mathcal{A} = \oint |\nabla r| \mathcal{J} d\theta d\zeta$. Non-axisymmetric magnetic perturbation fields generate both intrinsically ambipolar Γ_a and non-intrinsically ambipolar flows Γ_{na} . Ambipolar transport $\Gamma_a = \Gamma_{\bar{V}} + \Gamma_E + \Gamma_R$ is caused by center of mass parallel flow \bar{V} , $V_E = E \times B / B^2$ flow, and collisional transport. Non-ambipolar transport $\Gamma_{na} = \Gamma_V - \Gamma_{\bar{V}} + \Gamma_p + \Gamma_{pol} + \Gamma_\pi$ is caused by relative parallel flow, diamagnetic flow, and the drifts due to non-inertial and viscous forces. In equilibrium, the electric field will reach the value required for ambipolar transport E_A so that both $\Gamma_A \equiv \Gamma_a(E_A)$ and $\Gamma_{NA} \equiv \Gamma_{na}(E_A)$ are ambipolar and the net flux is equal for electrons and ions. The small electron/ion mass ratio $m_e/m_i \ll 1$ implies that electrons dominate parallel conduction processes due to their larger thermal velocity and ions dominate perpendicular conduction processes due to their larger gyroradius. Thus, ambipolarity implies that, to lowest order,

$$\langle \Gamma_{NA} \rangle \simeq \langle \Gamma_{J,e} + \Gamma_{p,e} \rangle \simeq Z_i \langle \Gamma_{p,i} + \Gamma_{pol,i} + \Gamma_{\pi,i} \rangle. \quad (13)$$

4 Plasma response

A plasma can react to an external magnetic perturbation in a manner that both suppresses and amplifies the perturbation simultaneously. Three complex “transmission factors” are sufficient to parameterize the effect of the ideal and non-ideal physics at play. These transmission factors are required to estimate quasilinear transport in Sec. 5. Ideal MHD determines many aspects of the plasma response for perturbations that travel slowly compared to the Alfvén speed. The linear ideal MHD response, described in Sec. 4.1, allows one to define two solutions far from a rational surface: a small solution that can produce no tearing and a large solution that may. The ratio of the two solutions is determined by the physics in the layer, which may require non-ideal effects for an accurate description. In general, the layer physics can be complicated, but the effect can be parameterized with two complex parameters defined in Sec. 4.1: the relative internal transmission factor S_{int} , which quantifies the screening by the current channel, and the relative transmission factor for reconnection S_{rec} , which quantifies the screening within the current channel.

The absolute transmission factors are defined as the ratio between the perturbation in the plasma and the vacuum field perturbation. The external transmission factor \mathcal{T}_{ext} is completely determined by the linear ideal MHD response, which typically leads to an amplification of the least stable modes of the system, as described in Sec. 4.2. This so-called “resonant field amplification” leads to an external transmission factor \mathcal{T}_{ext} that can be larger than unity and amplifies the tearing that would occur if the shielding currents were to relax. Because the absolute internal transmission factor $\mathcal{T}_{int} = S_{int} \mathcal{T}_{ext}$ and the absolute reconnection transmission factor $\mathcal{T}_{rec} = S_{rec} \mathcal{T}_{int}$ are both proportional to \mathcal{T}_{ext} , resonant field amplification (RFA) always plays an important role in determining the ELM control threshold, regardless of the details of the processes involved. This leads to the conclusion that there is a window in plasma β (actually in the local gradient α) over which ELM suppression should occur.

The linear two-fluid drift-MHD plasma response, discussed in Sec. 4.3, generates resonances in the relative transmission S_{int} at the $E \times B$ frequency and the ion and electron diamagnetic frequencies $\omega_{*,i,e}$. The addition of diffusion in the so-called semi-collisional regimes tends to smooth the $E \times B$ and ion resonances, but cannot affect the electron resonance, which is determined by the parallel Ohm’s law. Thus, an island can form most easily near the location where the electron impedance nearly vanishes, which is near the location where the relative perpendicular electron rotation $\omega_e \equiv \omega - \omega_{*e}$ vanishes.

4.1 Ideal MHD response near a rational surface

Plasma physics is well-described by ideal MHD sufficiently far from a rational surface r_s where the perturbation wavenumber \mathbf{k} matches the “pitch” of the equilibrium magnetic field \mathbf{B}_0 . On this surface, the safety factor is a rational number $q(r_s) = m/n$ and the pitch-resonant component of the perturbed flux, which satisfies $k_{\parallel} \propto m - qn = 0$ can potentially cause an magnetic island to form. However, an ideal conductor must conserve the

evolution of magnetic flux through any closed loop that moves with the conductor. Reconnection is forbidden in an ideal conductor because a topological rearrangement of magnetic field lines requires an essential redistribution of magnetic flux. In a plasma, which is a nearly ideal conductor, a narrow current layer arises in the vicinity of the rational surface to shield the reconnected flux. Plasma rotation governs the nonlinear and/or dissipative processes that determine the structure of the surface current layer. Because reconnection generically breaks magnetic surfaces and causes a loss of plasma confinement there are essentially two plasma states: a state of good confinement where temperature is high and resistivity is low and little reconnection is possible and a state of poor confinement where temperature is low and resistivity is high and reconnection can proceed freely.

The physics near the rational surface simplifies in the limit of zero pressure and large aspect-ratio slab geometry. Assume that there is symmetry, so that the perturbation depends only on $y = \theta - \zeta n/m$ and is independent of $z = \zeta$. The helical flux is defined as $\psi \equiv \psi_z = \psi_\zeta - \psi_\theta n/m \simeq B_0 x^2 / 2L_s + \delta\psi(x) \exp(imy)$. The flute-reduced MHD equations [67] evolve the magnetic field $\mathbf{B} = B_0(\mathbf{z} + \mathbf{z} \times \nabla\psi)$ and guiding-center velocity $\mathbf{V} = \mathbf{z} \times \nabla\phi/B_0$. The equations are written using MHD normalization for the variables defined by an arbitrary radial scale length r_0 , density n_0 and reference Alfvén velocity $V_{A0}^2 = B_0^2 Z_i / \mu_0 n_0 m_i$, where μ_0 is the magnetic permeability. The normalized variables are $\hat{B} \equiv B/B_0$, $\hat{\psi} \equiv \psi/B_0 r_0$, $\hat{\phi} \equiv \phi/B_0 r_0 V_{A0}$, $\hat{V} = V/V_{A0}$ and $\hat{t} \equiv V_{A0} t/r_0$. Dropping the hats for ease of notation, the Ohm's law and current continuity (vorticity) equations become

$$\partial_t \psi = -[\phi, \psi] \quad (14)$$

$$\partial_t U = -[\phi, U] - [\psi, J] \quad (15)$$

$$U = \nabla \cdot V_A^{-2} \nabla \phi \quad (16)$$

$$J = \nabla^2 \psi \quad (17)$$

$$[A, B] = \mathbf{z} \cdot \nabla A \times \nabla B. \quad (18)$$

Let ω_L be the perturbation frequency in the lab frame and $\omega_E = k_y V_E$ be the $E \times B$ frequency due to the equilibrium electric potential $\phi_0(r)$. Far from the rational surface, the dispersion relation allows shear Alfvén waves $\omega^2 \equiv (\omega_L - \omega_E)^2 = (k_{\parallel} V_A)^2$. The system also reduces the fast compressional Alfvén wave to the two solutions of the vacuum dispersion relation, $k_{\perp}^2 = 0$. The non-singular “vacuum solution” $\psi_{vac}(r) \propto r^m \exp(imy)$, shown as the dashed green curve in Fig. 3, is the solution that would be generated by a perturbation on the boundary $\psi_{vac}(a)$ if there were no plasma. Magnetic shear causes the two Alfvén branches to mode-couple in the vicinity of the rational surface when $\omega \neq 0$. In the region exterior to the Alfvén resonances, the physics asymptotically limits to the decoupled case and allows one to define the two canonical solutions that are required for the rest of the analysis. For non-ideal models, the width of the response layer w is set by physics other than the Alfvén resonances, so w will be considered to be an independent parameter in the following. At the end of this subsection, the linear ideal MHD response in the mode-coupling region between Alfvén resonances will be described in detail.

Even in the general case where the interchange and kink instabilities are retained, two linearly independent ideal solutions can be defined in the exterior region. (i) The free-boundary *exterior* solution ψ_{ext} (blue, dotted curve), also known as the small solution, is defined so that it produces no tearing: it is non-zero on the boundary $r = a$ and vanishes at the rational surface $r = r_s$. In a symmetric slab or cylinder, there is no coupling between Fourier harmonics and $\psi_{ext}(r < r_s) = 0$. To normalize this solution to the vacuum solution, let $\psi_{ext}(a) = \psi_{vac}(a)$. (ii) The fixed-boundary *interior* solution ψ_{int} (red, dotted curve), also known as the large solution, is defined to be produced by a current on the rational surface: it vanishes on the boundary $\psi_{int}(a) = 0$ and is non-vanishing at the rational surface. Thus, this solution can potentially produce tearing of the flux surfaces. As shown in Fig. 3, both solutions have a cusp at the rational surface determined by the jump in the radial derivative

$$[\psi'] \equiv \lim_{x \rightarrow +w} \psi'(r_s + x) - \psi'(r_s - x). \quad (19)$$

The cusp represents a surface current on the rational surface. To normalize the interior solution, let the cusp in the solutions be equal and opposite to that of the external solution $[\psi'_{int}](r_s) \equiv -[\psi'_{ext}](r_s)$. The general solution (solid black curve) in the exterior region defined by $|r - r_s| \gg w$, where w is the width of the current layer can be expressed as the linear combination

$$\psi(r) = \Psi_{int}\psi_{int}(r) + \Psi_{ext}\psi_{ext}(r). \quad (20)$$

The relative transmission factor is defined to be $\mathcal{S}_{int} = \Psi_{int}/\Psi_{ext}$. For example, if $\Psi_{int} \propto \mathcal{S}_{int} = 0$, then the solution is clearly ideal. On the other hand, if $\mathcal{S}_{int} = 1$, so that $\Psi_{int} = \Psi_{ext}$, then the surface current apparently relaxes and the solution is proportional to the smooth “relaxed” solution $\psi_{relax}(r) = \psi_{ext}(r) + \psi_{int}(r)$ (solid purple curve). In this case, the ratio of the internal flux to the vacuum flux is $\mathcal{T}_{ext} = \psi_{int}(r_s)/\psi_{vac}(r_s)$, and is typically amplified by toroidal effects as discussed in the next section. Note, however, that because the exterior/small solution is most easily extracted from an ideal MHD code, the external transmission factor is often estimated via the approximation $\mathcal{T}_{ext} \simeq -[\psi'_{ext}(r_s)]/2\psi'_{vac}(r_s)$. While \mathcal{T}_{ext} is determined by the properties of the ideal MHD solution in the exterior region alone, the internal transmission factor $\mathcal{T}_{int} = \mathcal{S}_{int}\mathcal{T}_{ext}$ is determined by the physics near the rational surface.

The ideal solution requires a net surface current to flow near the rational surface that can be measured by the cusp in the solution

$$\Delta' \equiv [\psi']/\bar{\psi} = \lim_{x \rightarrow w} \int_{r_s-x}^{r_s+x} \mu_0 J e^{-imy} d^3x / \mathcal{A}\bar{\psi}. \quad (21)$$

Given the normalizations above, the traditional tearing stability parameter is $\Delta'_{int} = -\Delta'_{ext} = [\psi'_{int}]/\psi_{int}$ (with instability if $\Delta'_{int} < 0$). The equation

$$\Delta' = \Delta'_{int}(1 - \Psi_{ext}/\Psi_{int}) \quad (22)$$

can be restated as a complex equation for the relative transmission of the internal solution

$$\mathcal{S}_{int} = 1/(1 - \Delta'/\Delta'_{int}). \quad (23)$$

The radial structure of the current near the rational surface is determined by the physics active in the inner layer. Each Fourier harmonic of J in Eq. 21 must match the asymptotic boundary condition determined by Δ'_{int} in Eq. 22. Since plasma rotation at frequency ω (relative to the rest frame of the perturbation) tends to suppresses reconnection, typically, $1/|\mathcal{S}_{int}| \propto 1 + (\omega/\omega_{rec})^\alpha$ where ω_{rec} is a threshold frequency for reconnection.

Although the ideal solution ψ_{int} has tearing parity, it may or may not signify actual reconnection depending on the physics within the current channel near the rational surface. For the so-called “constant-psi” regimes, the solution for ψ does not vary much within the interior layer and $\psi(r_s) \simeq \Psi_{int}$. However, nearly-ideal regimes are not “constant psi,” which implies that the current layer has substructure. For these cases, the actual reconnected flux $\psi(r_s) \equiv \Psi_{rec}\psi_{int}(r_s)$ is much smaller than the asymptotic value at distances larger than the layer width

$$\bar{\psi}(r_s) \equiv \lim_{r \rightarrow w} (\psi(r_s+r) + \psi(r_s-r))/2 = \Psi_{int}\psi_{int}(r_s). \quad (24)$$

For nearly ideal regimes, the relative transmission for reconnection $\mathcal{S}_{rec} \equiv \psi(r_s)/\bar{\psi} = \Psi_{rec}/\Psi_{int}$ and the total transmission for reconnection $\mathcal{T}_{rec} \equiv \mathcal{S}_{rec}\mathcal{T}_{int} = \mathcal{S}_{rec}\mathcal{S}_{int}\mathcal{T}_{ext}$ are typically rather small. The actual island width of the island that would be generated is $w_{rec} = 4\sqrt{|\psi(r_s)L_s/B_0|} = w_{vac}\sqrt{|\mathcal{T}_{rec}|}$.

The linear ideal MHD response [56] to an external perturbation is the canonical example of a “non-constant psi” regime [22]. Assume that the background helical flux possesses magnetic shear so that $\psi_0/B_0 = x^2/2L_s$ and $k_{\parallel} = k'_\parallel x = k_y x/L_s$. The ideal MHD constraint $E_{\parallel} = 0$ implies that $\delta\phi = \delta\psi\omega L_s/c k_y x$, where the relative frequency is $\omega = \omega_L - \omega_E$. For a thin perturbation $\partial_x \gg k_y$, the dispersion relation is $\partial_x [\omega^2 - (V_A k_{\parallel})^2] \partial_x \delta\phi = 0$. Thus, the compressional wave couples to the shear Alfvén wave at the two locations $\pm x_A$ where $x_A = \omega/k'_\parallel V_A = \omega/\omega_A k_y$ and $\omega_A = V_A/L_s$. For example, for drift frequencies $\omega_{*n} = k_y \rho_{cs} V_s/L_n$, where the ion sound speed is $V_s = \sqrt{(T_e + T_i)/m_i}$ and $1/L_n = d \log n/dx$, the resonance spacing $x_* \sim \rho_{cs} \sqrt{\beta} L_s/L_n$ is typically on the order of the ion sound gyroradius $\rho_{cs} = V_s/\omega_{ci}$. The linearly increasing solution $\psi_{ext} = x$ represents the solution to an odd displacement of the flux surfaces at large distances, and, thus, is equivalent to the exterior solution. The interior solution is a constant $\psi_{int} = 1$, which represents the small solution in the slab. The response to an even displacement of the flux surfaces at large distances $\delta\psi = \text{Re}(2ix/\pi) \tanh^{-1}(x/x_A) \exp(ik_y y)$ is singular at the resonances x_A . As expected from ideal MHD, there is no reconnection at all: $\mathcal{S}_{rec} = 0$, because, as $x \rightarrow 0$, the flux vanishes as $\psi \sim x^2$. The interior solution for $|x| > x_A$ is actually phase-shifted by $\pi/2$ from the exterior solution. The asymptotic behavior as $x \rightarrow \infty$ is $\delta\psi \rightarrow |x| \cos(k_y y) + 2x_A/\pi \sin(k_y y)$. With the results $\Delta' = i\pi/x_A$ and $\Delta'_{int} = -\Delta'_{ext} = -2k_y$, the transmission factor becomes $\mathcal{S}_{int} = 1/(1 + i\pi\omega_A/2\omega)$. Thus, for the linear ideal case, $\mathcal{S}_{int} \ll 1$ for slow rotation $\omega \ll \omega_A$, but approaches 1 in the limit of large rotation $\omega \gg \omega_A$, even though $\mathcal{S}_{rec} = 0$.

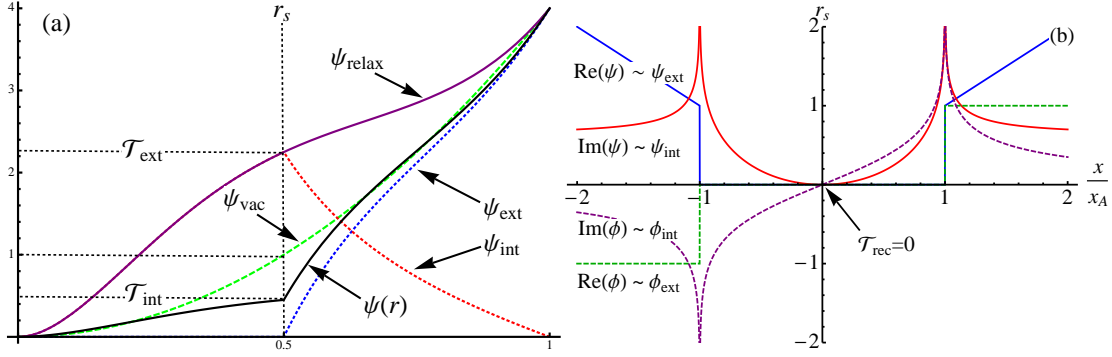


Fig. 3 (a) Magnetic flux ψ functions in the ideal external region $|r - r_s| \gg w$. The general solution $\psi(r)$ (solid black) is a linear combination of the ideal exterior ψ_{ext} (dotted blue) and ideal interior ψ_{int} (dotted red) solutions. In this case, the fully relaxed solution ψ_{relax} (solid purple) is less stable than the vacuum solution ψ_{vac} because $|\mathcal{T}_{ext}| > 1$. However, inner layer physics keeps the internal transmission factor $\mathcal{T}_{int} \ll 1$. (b) The magnetic flux ψ (solid) and electric potential ϕ (dashed) in the inner region $|r - r_s| \ll w$ for a “non-constant” ψ regime has multiple layers. The ideal inertial regime displays Alfvén resonances at $r - r_s = \pm x_A$, but the flux vanishes at r_s so there is no reconnection $\mathcal{T}_{rec} = 0$. The relative transmission factor S_{int} reduces the interior component and generates a phase delay of $\pi/2$. $\text{Re}(\psi) \propto \psi_{ext}$ (blue) implies that $\text{Im}(\psi) \propto \psi_{int}$ (red).

4.2 Resonant amplification of the exterior solution

Any external perturbation that is resonant with an ideal MHD normal mode will be amplified within the plasma due to “resonant field amplification” (RFA) [57]. In axisymmetric toroidal geometry, the poloidal harmonics of the ideal MHD eigenfunctions couple and the ideal solutions develop a cusp, as shown in Fig. 3(a), in the vicinity of all rational surfaces for a given n . In addition, finite current and pressure gradients alter the mode structure significantly from the vacuum case. For an ideal plasma, the plasma displacement $\xi = \delta\mathbf{x}(\psi, \theta, \zeta)$ can be taken to represent the plasma state. If $\hat{\mathbf{F}}$ represents the linearized MHD force operator, the linear response of a plasma can formally be decomposed into normal modes $\hat{\mathbf{F}}\xi_\lambda = -\omega_\lambda^2 \rho \xi_\lambda$ where here $\rho = m_i n_i$. The response to any external source $\mathbf{S}(x)e^{-i\omega t}$, determined by the solution to $\rho\ddot{\xi} - \hat{\mathbf{F}}\xi = \rho\mathbf{S}(x)e^{-i\omega t}$, can be formally represented as $\xi = \sum_\lambda \langle \xi_\lambda^\dagger \cdot \mathbf{S} \rangle e^{-i\omega t} \xi_\lambda / (\omega_\lambda^2 - \omega^2)$ where, here, $\langle X \rangle = \int X \rho d^3x$ denotes the inner product over the volume. Since the external perturbation is typically much slower than the Alfvén frequency, $\omega \ll \omega_\lambda \sim \omega_A$, if the least stable, i.e. lowest frequency, mode approaches marginal stability $\omega_0^2 \rightarrow 0$, a very large response will be elicited for a relatively small perturbation $\xi \simeq \langle \xi_0^\dagger \cdot \mathbf{S} \rangle e^{-i\omega t} \xi_0 / (\omega_0^2 - \omega^2)$. For example, the least stable ideal mode is often an external kink mode (stabilized by an external wall), which becomes unstable when $\beta_n = \beta a B^2 / I_{tor} B_{tor}$ exceeds the stability limit $\beta_{crit} \sim \mathcal{O}(1)$. Thus, amplification scales as $\mathcal{T}_{ext} \propto 1/(1 - \beta_n/\beta_{crit})$. Near marginal stability, the singular behavior of the transmission factor will be resolved by non-ideal and/or nonlinear effects.

Observation of RFA has been confirmed experimentally in studies of resistive wall modes on both DIII-D [58] and JET [59]. The first detailed investigations were made using the CAS3D code to predict the size of islands caused by error fields in W7X [60, 61]. Ideal linear response calculations also give information about the possibility of stochasticity because, if nonlinear effects are small, the island size that would be generated if there were no plasma screening can be determined from the magnitude of the shielding current near the rational surface. The first investigations for tokamaks were made using the IPEC code [62], based on the DCON eigenvalue code [63], to determine the non-axisymmetric deformation of tokamak equilibria due to magnetic perturbations. It was found that the ideal MHD response for plasmas of interest will often substantially rearrange the applied field spectrum from the vacuum field. Perturbation fields that match the eigenmodes are strongly amplified and such harmonics need to be targeted for error field control [64], and for ELM control, as well. The nonlinear plasma response has also been calculated using the initial value MHD codes NIMROD [31], M3D [32] and using the MARS-F code [48, 52, 65, 66]. For resistive MHD models, sufficiently strong plasma rotation should reproduce the ideal limit. However, as shown below, drift-MHD models are necessary to accurately describe the non-ideal physics in the H-mode pedestal.

RFA represents a resonance between the applied field and the ideal MHD eigenmodes $\omega = \omega_\lambda$ and should not be confused by the “pitch”-resonance condition for reconnection $k_\parallel = 0$. However, amplification of the internal flux ψ_{int} relative to the applied field ψ_{vac} also amplifies both Ψ_{ext} and Ψ_{rec} . Thus, a critical threshold to achieve ELM control that depends on the size of the perturbation in the plasma, whether it be Ψ_{ext} , Ψ_{int} , or Ψ_{rec} , also implies that there must be a critical threshold in external amplification \mathcal{T}_{ext} . A corollary implies that there is a critical threshold in normalized pressure gradient $\alpha > \alpha_{control}$ in order to achieve sufficient amplification for ELM control. If α becomes too large (and the pedestal is not entirely in the second-stable region), then the edge pressure will again violate the ELM stability criterion α_{ELM} . Thus, ELM control will typically only be achievable within the window $\alpha_{ELM} > \alpha > \alpha_{control}$. Consideration of RFA is important for achievement of ELM control and for the design of the perturbation spectrum because there is an upper limit on the perturbation amplitude that can be applied due to constraints imposed both by engineering and plasma physics. Above a critical perturbation strength, sufficient viscous damping will be generated to lock the plasma rotation to the perturbation frequency [22] and can cause termination of the discharge. Recent experiments on MAST [48] demonstrate that sculpting the ideal MHD response spectrum in order to produce a large amplification at the plasma edge generates an internal field structure that affects the edge without locking core rotation. The opposite condition, amplification near the more dangerous low-order rational surfaces, often caused a back-transition to L-mode [48, 52, 53]. Hence, altering the edge q -profile and plasma shaping can strongly impact the amplification for a given perturbation, and thus, impact the ability to achieve ELM control with a given perturbation spectrum.

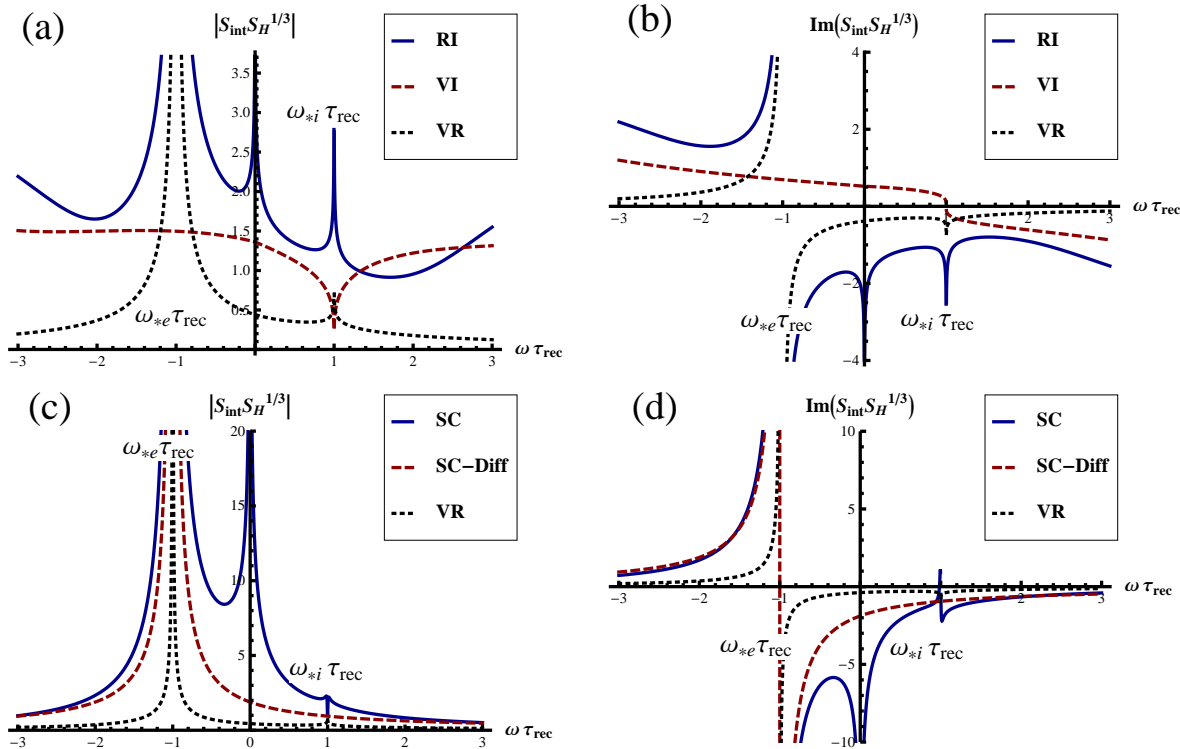


Fig. 4 The transmission factor for linear solutions to the drift-MHD equations, scaled by $S_H^{1/3}$ for $m = 1$. Drift frequencies are assumed to be rather slow $\omega_{*i}\tau_{rec} = -\omega_{*e}\tau_{rec} = 1$ to emphasize the resonances. (a) Amplitude and (b) imaginary part for 2 fluid-MHD regimes: resistive-inertial (RI, solid blue), visco-inertial (VI, dashed red), and visco-resistive (VR, dotted black) cases. (c) Amplitude and (d) imaginary part for FLR regimes $\rho_{cs} = 5\rho_{rec}$: non-diffusive semi-collisional regime (SC, solid blue, $P_D = P_\mu = 0$); diffusive semi-collisional (SC-Diff, dashed red, $P_D = P_\mu = 100$), compared to visco-resistive (VR, dotted black).

4.3 Non-ideal plasma response

The non-ideal response of the plasma near the rational surface is determined by nonlinearity, dissipative processes and finite Larmor radius (FLR) effects, and, in turn, determines the deviation of both \mathcal{T}_{int} and \mathcal{T}_{rec} from the linear ideal solution. Depending on the character of the dominant impedance mechanism, an island may or may not be allowed to form. The theory and observation of magnetic islands was recently reviewed in [68]. The asymptotic linear analysis was reviewed for single-fluid MHD in [22] and extended to isothermal two-fluid drift-MHD in [69]. Ref. [70] extended the drift theory to include classical diffusion, and arbitrary particle diffusivity is studied in [35]. The extension of the analysis to include neoclassical flow damping and the bootstrap current was performed in [71, 72, 73].

If an island does form, the fast parallel transport tends to flatten the electron temperature gradient across the island. Thus, isothermal models can be considered with some justification. Many authors have studied the 4-field reduced drift-MHD single-helicity model [67, 76] which determines the fields $\mathbf{B} = (B_z \mathbf{z} + \mathbf{z} \times \nabla \psi)$ and $\mathbf{V} = V_z \mathbf{z} + \mathbf{B} \times \nabla \phi$. Within the “flute-reduced” ordering, curvature changes occur at second order $\delta(\mathbf{b} \cdot \nabla \mathbf{b}) \sim \mathcal{O}(\delta^2)$, which implies that $\delta B_z / B = -\mu_0 \delta p / B^2 = -\beta \delta p / 2p_0$ where $\beta = 2\mu_0 p / B_0^2$. To describe the model, introduce dissipative terms: anomalous diffusivity D_0 , kinematic viscosity μ , and resistive diffusivity $\eta_{||}/\mu_0$ and define the additional normalizations: $\hat{T} = T/eBr_0V_{A0}$, $\hat{p}_j \equiv \hat{n}\hat{T}_j$, $\hat{V} = V_z/V_{A0}$, $\hat{D} \equiv D_0/V_{A0}r_0$, $\hat{\mu} \equiv \mu/V_{A0}r_0$, and $\hat{\eta} = \eta_{||}/\mu_0 V_{A0}r_0$. After dropping the hats for ease of notation, the normalized equations become

$$\partial_t \psi = -[\phi - T_e \log n, \psi] + \eta J \quad (25)$$

$$\partial_t U = -\nabla \cdot [\phi + T_i \log n, V_A^{-2} \nabla \phi] - [\psi, J] + \nabla \cdot \mu \nabla (U + \nabla^2 T_i n) \quad (26)$$

$$\partial_t n = -[\phi, n] + [\psi, nV + \rho_{cs}^2 J] + \nabla \cdot D \nabla n \quad (27)$$

$$\partial_t nV = -[\phi, nV] + [\psi, \beta n]. \quad (28)$$

Here, the gyroviscous cancellation given by Ref. [67] results in the first (advective) term on the RHS of Eq. 26. Matching to the ideal external solution as $x \rightarrow \infty$ implies $\psi \rightarrow (A_0 + A_1 k_y |x|) e^{ik_y y}$, $\phi \rightarrow \psi \omega L_s / c k_y x$ and $n \rightarrow \phi \omega_* / \omega$, $V \rightarrow 0$.

A comparison of the relevant time scales, shown in Fig. 2(a), is necessary to distinguish the importance of the various terms in these equations. It is common to define the Lundquist # (or magnetic Reynolds #) as the ratio between the Alfvén time $\tau_A = qR/nV_{A0}$ and the resistive time, $\tau_R = r_s^2 \mu_0 / \eta_{||}$ so that $S_A = \tau_R / \tau_A$. In fact, the actual dimensionless parameter that appears in the theory is the hydrodynamic time associated with the magnetic shear $\tau_H = L_s/nV_{A0}$. As can be seen in Fig. 2(b), the physically relevant definition of the Lundquist number $S_H = \tau_R / \tau_H$ (solid black curve) is typically a bit larger than S_A (dashed black curve), because $L_s = qR/s$ is typically smaller than qR at the edge, where the shear is large. The “Prandtl #’s” are defined as the ratio between the anomalous diffusivities and the resistive diffusivity: $P_\mu = \mu \mu_0 / \eta_{||}$ and $P_D = D_0 \mu_0 / \eta_{||}$. When the anomalous viscosity is estimated from the energy confinement time, the Prandtl # is of order 10-100, implying that the effect of anomalous diffusivity is relatively important. For example, Fig 2(a) and (b) compares the time scales and Prandtl #’s estimated from the T_i profile (solid blue line) to that defined using a constant value of $1 \text{ m}^2/\text{s}$ (dashed blue line). Finally, the ratio of ρ_{cs} to the visco-resistive layer width $\rho_{rec} = S_H^{-1/3} r_s$ describes the importance of FLR terms. As can be seen in Fig. 2(b), FLR terms are significant because $R_H = \rho_{cs} / \rho_{rec} \sim 5 - 10$ (solid red). This conclusion holds even if computed using S_A (dashed red) instead of S_H . Since both $P > 1$ and $R > 1$ for this discharge, the so-called “semi-collisional” regimes are of greatest relevance (if anomalous transport is included).

Analytic dispersion relations for the linear three field model obtained by neglecting the sound wave coupling and setting $V \rightarrow 0$ have been studied in [69, 70, 35]. Fig. 4(a) shows the relative internal (yellow) and reconnected (magenta) transmission factors, and the total reconnected transmission factor (blue) for the visco-inertial regime. Fig. 4(b) shows the reconnected flux for the inviscid ($D = \mu = 0$) regime (blue), for the visco-inertial regime (magenta) and the visco-resistive regime (yellow). Figures 4(c) and (d) compare results for the semi-collisional inviscid case (blue), the diffusive semi-collisional case (magenta) and the visco-resistive case (yellow) assuming $P_D = P_\mu = 100$.

Dissipation generally smooths both the ion and gyro-center resonance. However, the electron resonance is robust to these effects precisely because this is the point where the electron impedance for driving parallel current is minimized and nearly vanishes. In fact, 8 out of 10 regimes (all non-inertial regimes) identified in Ref. [70]

have Δ 's that depend more strongly on $\omega_e \equiv \omega - \omega_{*e}$ than on $\omega_i \equiv \omega - \omega_{*i}$ (see Table I of Ref. [70] but note the different notation used there). The explanation is easiest to understand after transforming the parallel Ohm's law to Fourier space. The helical flux is determined via $(\omega - \omega_{*e} + i\eta k^2)\psi_k = \dots$ which yields the largest result when the perpendicular electron frequency ω_e vanishes. In a low-collisionality plasma, the resistance (real part) is much smaller than the reactance (imaginary part) unless $|\omega_e| < \eta k^2$. Both linear [30] and nonlinear [34] simulations have confirmed the ability of islands to form near this location. Note, however, that Refs. [30, 83] have determined a kinetic correction to the electron diamagnetic frequency that is proportional to the electron temperature gradient. Fig. 4 clearly shows that the Lorentz force, proportional to the transmission factor $\text{Im } \mathcal{S}_{int}$, changes sign when $\omega_{*e} < \omega < \omega_{*i}$. The force always acts to brake electrons, but this will act to increase ion rotation when electrons and ions rotate in opposite directions relative to the perturbation; i.e. when $\omega_e \omega_i = (\omega - \omega_{*e})(\omega - \omega_{*i}) < 0$.

5 Steady-state transport mechanisms

The effect of small perturbations on transport can be estimated from the second-order nonlinear, i.e. quasilinear, response. As shown in Sec. 5.1, the quasilinear convective transport due to magnetic perturbations, the so-called "magnetic flutter flux" (Eqs. 31 and 32), is proportional to the quasilinear Lorentz force. Both the force and the flux depend on \mathcal{T}_{ext} and can change direction because they are proportional to $\text{Im } \mathcal{S}_{int}$. In the core, where electrons and ions rotate in the same direction, the force acts to decelerate the flow and the flux acts to increase particle confinement. In the pedestal, where electrons and ions rotate in the opposite direction, the force acts to decelerate the electrons and accelerate the ions and the flux acts decrease the particle confinement. The predictions are qualitatively similar to observations in the case (ii) low-collisionality ELM suppression regime discussed in Sec. 2. The effect generates a jump in the equilibrium density profile that becomes significant at a threshold in field amplitude determined by the background diffusivity (Eq. 35). The quasilinear structure of the layer is completed in Sec. 5.2 after consideration of ion viscous forces.

Transport mechanisms that incorporate physics beyond the drift-MHD model of Sec. 4 are considered next. The ion viscous force, which plays a key role in particle transport, is typically dominated by neoclassical poloidal flow damping. As shown in Sec. 5.2, this can potentially yield particle transport that is $\sqrt{m_i/m_e}$ times larger than the axisymmetric case if there is a non-ambipolar electron transport mechanism that is simultaneously active. A stochastic magnetic field, determined by the reconnected flux \mathcal{T}_{rec} , naturally provides non-ambipolar electron transport. While stochasticity typically enhances electron transport, thermal transport will not dominate particle transport until a threshold in perturbation strength is exceeded (Eq. 50). Finally, results of calculations of stochastic transport for low-collisionality ELM-suppression cases are discussed in detail.

5.1 Quasilinear transport

Transport along flux surfaces can flatten the gradients of temperature and density radially across an isolated island. If the island width w approaches the ion gyroradius ρ_{ci} , the electrons will respond much more strongly to the magnetic structure than the ions. As the island width is increased, the electron temperature will flatten first, then the density and ion temperature gradients will follow. The critical width for each of these stages is determined by the condition for in-surface transport to dominate perpendicular transport across surfaces [78, 79]. The parallel electron particle transport channel is often referred to as "magnetic flutter flux." This flux was first shown to be capable of inverting the density gradient across an island in the computations of Refs. [81, 82]. Since only electrons participate in the parallel current to $\mathcal{O}(m_e/m_i)$, there is an equivalent ion flux due to drifts generated by non-ambipolar forces such as inertia, viscosity, and ion-neutral collisions. As discussed in Sec. 3, this component is equivalent to $E \times B$ transport across flux surfaces.

The quasilinear flux can be derived in a manner that is similar to the derivation of the quasilinear Lorentz force integrated over the layer. The Lorentz force is determined by the Maxwell stress tensor $\mathbf{T}_{EM} = (\mathbf{B}\mathbf{B} - B^2/2)/\mu_0$ via $\nabla \cdot \mathbf{T}_{EM} = \mathbf{J} \times \mathbf{B}$. Just as the total Lorentz force can be expressed as $\int \mathbf{J} \times \mathbf{B} d^3x = \oint \mathbf{T}_{EM} \cdot d^2\mathbf{a}$, the flux-surface averaged torque density can be expressed as

$$\langle f_{EM,\theta} \rangle = \langle \mathbf{J} \times \mathbf{B} \cdot \partial_\theta \mathbf{x} \rangle = \langle \partial_r T_{EM,\theta}^r - \mathbf{T}_{EM} : \nabla \partial_\theta \mathbf{x} \rangle. \quad (29)$$

Asymptotic matching to the ideal exterior region implies that the total current integrated across the layer must be parallel to the equilibrium field. Thus, as derived in Sec. 3, both the jump in the tangential field $[B_\theta] = -q[B_\zeta]$ and the force across the layer $f_{EM,\theta} = -q f_{EM,\zeta}$ must be perpendicular to the equilibrium field. The result is

$$\langle f_{EM,\theta} \rangle = \langle \partial_r [B_\theta B^r / \mu_0] \rangle = \delta(r - r_s) \text{Im } \mathcal{S}_{int} |\mathcal{T}_{ext} B_{vac}|^2 / \mu_0 \quad (30)$$

where $B_{vac}^2 \equiv B_{r,vac} B^{r,vac}$. To derive this result, note that $[B^r B_\theta] = [\text{Re}(B_{int}^r B_{\theta,ext})] = B_{int}^r B_{r,int} \text{Im } \mathcal{S}_{int} = B_{vac}^r B_{r,vac} |\mathcal{T}_{ext}|^2 \text{Im } \mathcal{S}_{int}$. The second term on the RHS of Eq. 29 does not yield a contribution as singular as the first.

The quasilinear particle flux can be evaluated in two different ways $e\Gamma_{ql}^r = \langle J_{\parallel} \mathbf{b} \cdot \nabla r \rangle = -\langle \mathbf{J}_{\perp} \cdot \nabla r \rangle$. The two forms are a consequence of quasineutrality, which implies that the electron and ion fluxes are equal and opposite, as discussed in Sec. 3.3. The result is

$$\langle \Gamma_{ql}^r \rangle = \left\langle \frac{(B_\zeta \partial_r [B_\theta] - B_\theta \partial_r [B_\zeta]) B^r}{\mathcal{J}_e B^2} \right\rangle = \partial_r \left\langle \left[\frac{B_\theta B^r}{\mu_0 e \psi'_\theta} \right] \right\rangle = \delta(r - r_s) D_{ql} n_e \quad (31)$$

$$D_{ql} = \text{Im } \mathcal{S}_{int} |\mathcal{T}_{ext} B_{vac}|^2 / \mu_0 e n_e. \quad (32)$$

Equation 31 demonstrates the equivalence of both a direct computation of the parallel current and of substitution of the poloidal Lorentz force into Eq. 9. The characteristic ‘‘diffusivity’’ can also be written as $D_{ql} = \delta B^2 \text{Im } \mathcal{S}_{int} / \mu_0 e n_e = (2\rho_{cs} V_s / \beta) \times (\delta B / B)^2 \text{Im } \mathcal{S}_{int}$ where $\beta = 2\mu_0 p / B^2$. Investigation of the layer solution shows that the flow is actually convective with the characteristic radial flow $V_{ql} = D_{ql}/w$, where w is the width of the current channel. The particle flux critically depends (in Eq. 32) on the imaginary part of the relative transmission factor $\text{Im } \mathcal{S}_{int}$. As discussed in Sec. 3.3, the ion flux that determines \mathcal{S}_{int} is determined by viscous and non-inertial forces. In the core, the MHD assumption that the $E \times B$ frequency is much larger than the diamagnetic frequencies is valid. In this case, the force acts to decelerate both electrons and ions, and there is an inward particle flux. However, in the pedestal, the ions and electrons rotate in opposite directions over the entire red and green shaded region of Fig. 1(b). In this case, the force decelerates electrons, accelerates ions, and generates an outward particle flux. These relations are summarized in Fig. 5.

Linear and nonlinear island theory produces a rich variety of regimes and a variety of calculations of $\text{Im } \mathcal{S}_{int} \propto \text{Im } \Delta'$ have been performed in the literature, usually in the so-called ‘‘Rutherford’’ regime [69, 74, 75, 76, 77, 79, 80]. Since the torque is proportional to $\text{Im } \mathcal{S}_{int} \propto \text{Im } \Delta'$ this directly leads to predictions of the flux. For a combination of neoclassical and anomalous viscous forces, the torque scales with various combinations of the momentum damping rate [71, 72] and, hence, so does the flux. Note that the $E \times B$ flux across the unperturbed flux surfaces must be determined by integration over the radial structure in the inner layer. It cannot be directly evaluated by the asymptotic form of the solution because both ϕ and n_e each have the asymptotic scaling $\sim \psi/x$. This yields a large particle source in the inner layer and a vanishing flux $\sim 1/x^2$ far from the layer. It has been found to be small [35] unless the island size approaches the gyroradius in size, as discussed in Sec. 6.

In equilibrium, both the force and the flux must be balanced by other transport mechanisms. Total radial force balance leads to $[B^2/2\mu_0 + p] = 0$, so that there must also be a singular poloidal current

$$\mu_0 J_y / B = \partial_r [\mu_0 p] / B^2 = \delta(r - r_s) \beta [n_e] / n_e. \quad (33)$$

Particle continuity, Eq. 3, implies that if the magnetic flutter flux is balanced by an anomalous particle diffusion $V^r = -D_0 n'$, then integrating across the layer leads to a jump in density across the layer:

$$[n_e] / n_e = D_{ql} / D_0. \quad (34)$$

For a series of small jumps across N rational surfaces, the effect will become important once $N D_{ql} \sim D_0$. This yields a threshold

$$|\mathcal{T}_{ext}|^2 (\delta B_{vac} / B)^2 > \beta D_0 / N \rho_{cs} V_s |\text{Im } \mathcal{S}_{int}|. \quad (35)$$

Assuming $\beta \sim 10^{-3}$, $\rho_{cs} V_s \sim 10^3 \text{ m}^2/\text{s}$, and setting the transmission to order 1 would require $\delta B / B > 10^{-4}$ to exceed a background diffusivity of $0.1 \text{ m}^2/\text{s}$ over 10 surfaces. However, given the expected scaling of the transmission factor, the threshold would be $\mathcal{S}_{int}^{-1/2} \sim S_H^{1/6} \sim 30$ times larger, $\delta B_{vac} / B > 3 \times 10^{-3}$.

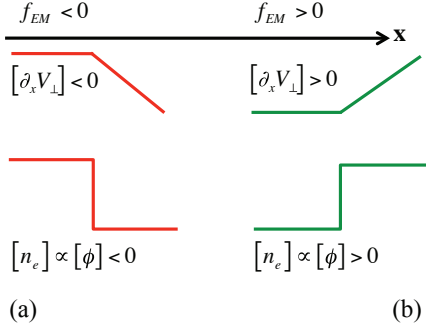


Fig. 5 Jump conditions for the case of anomalous toroidal viscosity. (a) In the core, where electrons and ions rotate in the same direction (unshaded region of Fig. 1(b)), the force acts to brake both species and generates an improvement in particle confinement. (b) In the pedestal, where electrons and ions rotate in opposite directions (shaded region of Fig. 1(b)), the force acts to brake electrons, generating a decrease in particle confinement.

5.2 Neoclassical transport

Neoclassical viscous transport, which is driven by the variation of $|B|$ within a flux surface, can compete with the low level of anomalous viscous transport in the H-mode edge. This is especially true for the low collisionality ELM suppression regime. Non-axisymmetric variations can directly drive transport through neoclassical toroidal viscosity (NTV) [84]. Perhaps surprisingly, the axisymmetric neoclassical poloidal viscosity (NPV) can also generate transport in reaction to the additional quasilinear forces and fluxes [36, 37]. Neoclassical theory predicts that the flux surface averaged components of the viscous force can be expressed as a viscous drag against the stationary field strength variations [84]

$$\langle f_{\pi,\alpha} \rangle = -\langle \partial_\alpha \mathbf{x} \cdot \nabla \cdot \boldsymbol{\pi} \rangle = -mn\mu_{nc} \sum_k k_\alpha (\langle \mathbf{k} \cdot \mathbf{V} \rangle \mathcal{I}_k[\delta B/B] + \langle \mathbf{k} \cdot 2\mathbf{Q}/5p \rangle \mathcal{L}_k[\delta B/B]) \quad (36)$$

where \mathbf{Q} is the heat flux, μ_{nc} is the kinematic viscosity, and the wave-vector $\mathbf{k} = M\nabla\theta - N\nabla\zeta$ refers to the Fourier harmonic of δB_\parallel . The form of the functionals $\mathcal{I}_k[\delta B/B]$ and $\mathcal{L}_k[\delta B/B]$ depend on the collisionality regime. For small perturbations, they scale as $(\delta B_\parallel/B)^2$ [84, 85], while for a sufficiently large island of width $w \propto \sqrt{\delta B_\perp/B}$ they scale as $\delta B_\parallel/B$ [86, 87].

Axisymmetric poloidal variations of the magnetic field strength yield a neoclassical poloidal viscous force (NPV). The usual analysis for a single ion species in large-aspect ratio geometry focuses on the parallel component of this force because there are no other significant parallel forces: inertia can be neglected, the ion viscous force is larger than the electron viscous force by $\sqrt{m_i/m_e}$, and friction forces vanish when summed over species. Thus, the parallel viscous ion stress must nearly vanish in order to satisfy parallel momentum balance and the neoclassical poloidal flow is determined by the neoclassical poloidal heat flux $V_{nc}^\theta \simeq -2k'_i Q_{nc}^\theta / 5p_i = -k_i T'_i / Z_{ieq}$. In a large aspect-ratio tokamak, $k_i = 1.7$ in the collisional regime, 0.5 in the plateau regime and -1.17 in the banana regime. Using radial force balance, the poloidal flow determines the radial electric field in the frame of reference that rotates with the plasma in the toroidal direction

$$\mathcal{E}_r \equiv -\phi' - V^\zeta \psi'_\zeta = p'_i/Z_i e n_i - q V^\theta \psi'_\zeta. \quad (37)$$

Neoclassical equilibrium is achieved rapidly and forces E_r to achieve the value

$$\mathcal{E}_{nc,i} = (p'_i/n_i + k_i T'_i + V^\zeta \psi'_\zeta)/Z_i e. \quad (38)$$

Due to axisymmetry, the toroidal flow V^ζ is nearly conserved and, hence, both V^ζ and ϕ evolve on a much slower timescale. Thus, the ion parallel viscous force and the ion particle flux $\Gamma_{\pi,i}^r$ are both suppressed by a factor $\sqrt{m_e/m_i}$, i.e. to the electron transport level [88, 89].

Additional forces due to inertia, anomalous viscosity, and ion-neutral friction can significantly modify the result of the usual neoclassical analysis. Parallel forces modify the equilibrium poloidal flow and nonambipolar perpendicular forces modify the radial electric conductivity [90, 91]. If the additional forces are primarily toroidal, then the net ion flux can potentially achieve the maximum value $\Gamma_{\pi,i}^r$. However, the magnitude of the ion flux, and therefore the net parallel force, is still constrained by ambipolarity, i.e. perpendicular force balance,

and would be forced to vanish if there were no other nonambipolar transport mechanisms. The addition of a nonambipolar electron transport mechanism can potentially enhance the neoclassical particle flux by a factor up to $\sqrt{m_i/m_e}$; i.e. to the ion transport level. Using Eqs. 9 and 36, the neoclassical radial fluxes are

$$\langle \Gamma_{\pi,i}^r \rangle = m_i n_i \nu_{nc,i} (V_{nc}^\theta - V^\theta) / Z_i e q \psi'_\zeta = D_{nc,i} n_i Z_i e (E_r - \mathcal{E}_{nc,i}) / T_i \quad (39)$$

$$\langle Q_{\pi,i}^r \rangle = \langle \Gamma_{\pi,i}^r \rangle T_i - \chi_{nc,i} n_i T'_i \quad (40)$$

where $\nu_{nc,i} \simeq \mu_{ii}/r_s^2$ is the poloidal flow damping rate, $D_{nc,i} \equiv \nu_{nc,i} \rho_{ci}^2$ is the ion diffusivity, and $\chi_{nc,i}$ is the thermal conductivity. In the Pfirsch-Schlüter regime $\nu_{nc,i} \sim q^2 \nu_{ii}$, in the plateau regime $\nu_{nc,i} \sim q V_{Ti}/R$, and in the banana regime $\nu_{nc,i} \sim \epsilon^{-3/2} q^2 \nu_{ii}$ where ν_{ii} is the ion-ion collision frequency [88]. If the normalized force becomes as large as $Z_i e (E_r - \mathcal{E}_{nc,i})/T_i \sim \mathcal{O}(1/L_n)$, then the effective diffusivity $D_{nc,i} \sim 0.05 - 0.5 \text{ m}^2/\text{s}$ is large enough to play a significant role in transport.

For a simple non-axisymmetric case, consider the quasilinear transport generated by an isolated magnetic perturbation discussed in the previous section. A common assumption [73, 77] is that the Lorentz force is balanced by neoclassical poloidal flow damping $f_{\pi,y} = -m_i n_i \nu_{nc,i} (V_y - V_{nc,y})$ and that parallel force balance is achieved through anomalous toroidal viscosity $f_{\pi,z} = m_i n_i \mu \nabla^2 V_z$. For the isothermal model, $V_{nc,y} \propto T'_i = 0$ and the force within the layer generates a singular poloidal flow

$$V_y/V_{Ti} = f_{EM,y}/m_i n_i \nu_{nc,i} V_{Ti} = \delta(r - r_s) \rho_{ci} D_{ql} / D_{nc,i}. \quad (41)$$

Total parallel force balance implies that the parallel component of the sum of the viscous forces must vanish, thereby generating a cusp in toroidal velocity

$$\rho_{ci,pol} [\partial_r V_{tor}] / V_{Ti} = D_{ql} / \mu. \quad (42)$$

where $\rho_{ci,pol} = \rho_{ci} B_{tor} / B_{pol}$. Radial ion force balance implies that

$$e(E_r - \mathcal{E}_{nc,i})/T_i = -\delta(r - r_s) D_{ql} / D_{nc,i}. \quad (43)$$

Thus, there must be a jump in the electric potential

$$e[\phi]/T_i = D_{ql} / D_{nc,i} - D_{ql} / D_0. \quad (44)$$

This requires the sign of the jump in density and potential to be proportional to the sign of the force in the layer, as shown in Fig. 5. Assuming that $D_0 > D_{nc,i}$ would yield the sign of the potential shown in the figure.

Non-axisymmetric variations in magnetic field strength directly generate a neoclassical toroidal viscous (NTV) force. This force can be large enough to determine the equilibrium toroidal flow because the axisymmetric NTV force is rather weak $\mathcal{O}(\delta^3)$ [92, 93]. The first analytic calculations of neoclassical transport induced by islands and resonant harmonics that were specifically for tokamak geometry were performed in Ref. [86]. Calculations of kinetic transport that include resonances between bounce and toroidal precessional motion and include the ideal MHD response fields in realistic geometry have been performed using IPEC [85]. The analysis of the low-collisionality regime showed that trapped particle resonances between the bounce frequency and toroidal precession frequency can cause a factor of ~ 100 times faster momentum damping than that expected from analytic estimates for the relevant $\nu - \sqrt{\nu}$ low-collisionality regime. MARS-K [94] has evaluated the kinetic effects on linear plasma response for RWM applications. If magnetic islands are negligible, the so-called “superbanana” plateau regime has been used to estimate the upper limit on NTV [84, 95]. Although the maximum NTV particle flux is relatively small, it can become large if magnetic islands open and become large enough to generate an NTV force that scales as $\delta B_{||}/B$ instead of $(\delta B_{||}/B)^2$.

5.3 Stochastic transport

If the flux surface topology is altered by magnetic islands or stochastic regions, parallel transport along the perturbed field lines will lead to a net radial flux with respect to the original flux surfaces [96, 23]. The quasilinear radial flux can be expressed in the form [97]

$$\langle \Gamma_e^r \rangle = D_{st,e} n_e e (E_{st,e} - E_r) / T_e \quad (45)$$

$$\langle Q_e^r \rangle = \langle \Gamma_e^r \rangle T_e - 2 D_{st,e} T'_e. \quad (46)$$

where

$$E_{st,e} = -p'_e/n_e - k_e T'_e. \quad (47)$$

For weakly collisional regimes, the distribution function remains close to a local Maxwellian and the cross-term varies between $k_e = 0.71$ (collisional) and $k_e = -0.5$ (plateau). Quasilinear theory [96] predicts that the diffusivity is limited to transport at the average thermal speed $D_{st} = D_{\parallel}(\delta B_{rec}/B)^2$ where the effective parallel diffusivity is $D_{\parallel} \simeq \sqrt{\pi/2}V_T qR$. Rechester and Rosenbluth [23] predicted that in the collisional regime transport occurs at the rate $D_{st,RR} = k_{RR}\sqrt{\chi_{\parallel}D_{\parallel}}(\delta B_{rec}/B)^2$ where k_{RR} is a prefactor that depends logarithmically on collisionality. Ref. [98] determines a variety of alternate prefactors that depend logarithmically on the dominant dissipation mechanism. The ion diffusivity is much smaller than the electron diffusivity since $D_{st,i}/D_{st,e} = V_{Ti}/V_{Te} \sim \sqrt{m_e/m_i}$. Hence, if parallel transport is dominant, the ambipolarity constraint will force the electric field to reach the value $E_{st,e}$ [97]. Because the heat flux satisfies Eq. 46, electron thermal transport remains $\sqrt{m_i/m_e} \sim 60$ times larger than the particle flux even when $\Gamma_e = 0$.

Quasilinear parallel transport scales as $D_{st} \sim \mathcal{T}_{rec}^2$, which depends sensitively on the reconnected flux. At 1 keV, the effective parallel diffusivities are $D_{\parallel,e} \sim 10^8 \text{ m}^2/\text{s}$ and $D_{\parallel,i} \sim 10^6 \text{ m}^2/\text{s}$ for deuterium. For $\delta B/B \sim 10^{-4} - 10^{-3}$, the quasilinear diffusivities are on the order of 1-100 m²/s and 0.01-1 m²/s, respectively. Since H-mode transport coefficients are typically on the order of 0.1-0.5 m²/s, the electron thermal diffusivity is far too large to fit measured profiles, but the particle and ion thermal diffusivities are in the range to compete with H-mode edge transport [27]. The first calculations of stochastic thermal transport in realistic divertor geometry [26, 27] were carried out for the DIII-D ELM control experiments using the E3D fluid transport code [99]. The magnetic field perturbations were taken to be equal to the vacuum field perturbations, and substantial thermal transport was generated, in good agreement with theoretical estimates. While the initial H-mode equilibrium state was in the collisionless regime, the final state had cooled sufficiently that it became collisional. Hence, the fluid calculation would have been valid *a posteriori* if the vacuum field assumption had been correct. The E3D calculation also observed clear changes to the heat flux near the strike point. The mapping of the invariant manifolds that intersect the X-point describe the envelope of the heat flux profile to the target plate [43]. The strike-point splitting is linear in the perturbation strength for small perturbations and can be described by Melnikov theory for small perturbations [27]. The E3D calculation clearly showed this structure, in agreement with the mapping. Subsequent studies using the EMC3-EIRENE fluid plasma/kinetic neutral transport code [28] also accounted for parallel flow V_{\parallel} along stochastic field lines, but did not account for the electric field. While particle transport was observed, the largest effect was in the reduction of the electron temperature. The implications of these studies are sufficient to exclude standard models of stochastic “vacuum” field transport.

When neoclassical transport is included in the analysis, reduced 1D and 2D transport modeling of ELM control discharges have shown that the deviation of \mathcal{E}_r from the neoclassical value can produce enough particle transport to describe experimental results [36, 37]. This requires the stochastic thermal transport to be suppressed by a factor of 30 – 100 over the vacuum approximation, which can be achieved through modest screening of the applied fields. For a combination of stochastic and neoclassical viscous transport, the ambipolar radial electric field and fluxes are determined by the value

$$E_{NA} = (\sigma_{st,e} E_{st,e} + \sigma_{nc,i} \mathcal{E}_{nc,i}) / (\sigma_{st,e} + \sigma_{nc,i}) \quad (48)$$

$$\langle \Gamma_{NA}^r \rangle = (E_{st,e} - \mathcal{E}_{nc,i}) / (\sigma_{st,e}^{-1} + \sigma_{nc,i}^{-1}) \quad (49)$$

where $\sigma_{st,e} = eD_{st,e}/T_e$ and $\sigma_{nc,i} = Z_i e D_{nc,i} / T_i$. Stochastic transport will dominate once $\sigma_{st,e} \gg \sigma_{nc,i}$. Thus, achieving large thermal transport would require a threshold in perturbation strength

$$\left(\frac{\delta B_{rec}}{B} \right)^2 > \frac{Z_j T_e}{T_i} \frac{D_{nc,i}}{D_{\parallel,e}} \simeq \frac{T_e}{T_i} \frac{\rho_{ci}}{qR} \frac{\nu_{nc}}{\omega_{ci}} \sqrt{\frac{2m_e}{\pi m_i}}. \quad (50)$$

If $\nu_{*i} \sim 1$ and $T_e \sim T_i$ at the separatrix, then the condition for thermal transport to exceed particle transport requires $\delta B_{rec}/B > (\rho_{ci}/qR)(2m_e/\pi m_i)^{1/4} > 10^{-5}$ for a deuterium plasma, assuming that $\rho_{ci}/qR \sim 10^{-4}$. Thus, the experimentally relevant applied fields would be in the correct range for enhanced particle transport rather than thermal transport if there is a modest screening of the vacuum fields, $\mathcal{T}_{rec} < 0.1$. However, the

experimental vacuum fields often generate weak stochasticity if there is no screening, and even a modest screening could eliminate island overlap.

Gyrokinetic simulations [29] of DIII-D discharge 126006 that used the vacuum field perturbation fields and allowed an ambipolar electrostatic potential $\phi_0(r)$, constrained to be a function of unperturbed flux surfaces, showed that the combined effects of particle trapping and heat flux limits reduced the magnitude of the stochastic heat flux by a factor of 8. The enhanced transport was still sufficient to destroy the pedestal profiles for temperature, density and the radial electric field. As predicted in [97], a large positive radial electric field developed in order to maintain ambipolarity, destroying the E_r well. Particle transport was roughly ~ 100 times larger than the unperturbed axisymmetric case due to parallel transport, non-axisymmetric parallel pressure variations, and NPV. Inside the pedestal the contributions from each channel were roughly equivalent, but the parallel pressure variation dominated at the separatrix. The simulations demonstrated that NPV transport $\Gamma_{\pi,i}$ in a stochastic field contributes a sizable fraction of particle transport, as large as parallel outflow Γ_V (as large as 1/3 of the total in Fig. 2(f) of [29]), and ~ 30 times larger than the axisymmetric case. The simulation [29] matches the analytic result well, but demonstrates that there are other significant components to the flux due to parallel outflow Γ_V and the non-axisymmetric pressure gradient Γ_p . Ref. [29] also explored an ad-hoc model for screening of the perturbation fields that produced results that were much more consistent with experimental data. If the magnetic perturbations are reduced in amplitude by a factor of 10 near the separatrix, so that the separatrix flux surfaces are retained, the electrons remain well confined by the flux-surfaces. In this case, large transport develops at the top of the pedestal, but not in the steep gradient region, and the profiles are in qualitative agreement with experiment. This indicates that screening of the perturbations in the steep gradient region is likely to be a good assumption. However, Sec. 4 demonstrated that screening is likely to be equally important across the entire pedestal. Thus, the underlying transport mechanism at the top of the pedestal is not necessarily due to a stochastic field, but perhaps due to a single island or a series of islands constrained to a small size by plasma response.

6 Interaction with turbulence

Experimental evidence suggests that there is a prompt impact on turbulent fluctuations during the application of the magnetic perturbations [39, 45]. The direct effect of the magnetic perturbation on the magnetic curvature drive is predicted to be small due to the tendency to develop field-aligned mode structure; i.e. within the flute-reduced ordering $\delta(\mathbf{b} \cdot \nabla \mathbf{b}) \sim \mathcal{O}(\delta^2)$ [67]. In fact, Ref. [100] actually found a reduction in the linear growth rate of drift waves due to the reduction in the density and temperature gradients across a sufficiently large island. However, Alfvén waves that develop a structure on the order of the ion gyro-radius can directly mode-couple to drift waves and can drive turbulent transport. Refs. [101, 102, 103] found that small-scale magnetic islands, with a width on the order of the ion gyroradius, actually radiate electron drift waves. This mechanism causes transport by drift waves that are not linearly unstable, but are driven by the island structure that develops. In the kinetic theory [101], radiation can propagate when the rotation lies in the electron drift band of frequencies $\omega_{e*} < \omega < 0$; i.e. as long as $\omega \omega_e < 0$. This region of the pedestal is shown as the green shaded region of Fig. 1(b). One failing of the drift-MHD model is that it allows drift wave propagation and radiation [102, 103] for $0 < \omega < \omega_{*i}$ as well, i.e. over the entire range $\omega_e \omega_i < 0$, the entire green and red shaded region in Fig. 1(b). Turbulent transport simulations including magnetic islands using the drift model have been explored numerically by [104, 105, 106].

In the steep gradient region of an H-mode pedestal, the flows are sheared strongly enough that they are believed to suppress turbulence. Sheared flows break apart smaller eddies by stretching the structure so finely that it eventually reaches length scales where dissipation provides strong damping. As described in Ref. [107] and references therein, many models of the impact of shearing predict that a sheared flow will reduce the anomalous diffusivity (proportional to turbulence amplitude) via $D_{turb} = D_0 / (1 + c|\omega_s/\gamma|^h)$ where $\omega_s = -\phi''_0/B$ is the flow shear frequency, γ is the decorrelation rate of the mode and c is a dimensionless parameter. The exponent $h = 2/3$ if the flow is laminar (linear shearing rate) and $h = 2$ if the flow has an X-point or is chaotic (exponential shearing rate). Ref. [108] derived a general non-Markovian model with $h = 2$, and a number of authors have found this scaling for particular models of turbulence. Thus, a reduction in equilibrium flow shear could lead to an increase in turbulent transport that would be of the correct order of magnitude to explain the experimental results.

Increased damping of zonal flow fluctuations would lead to a similar increase in turbulent transport [107]. Zonal flows suffer little collisionless damping because they vary radially, but have no toroidal or poloidal dependence to leading order. In simulation, these secondary instabilities are observed to be pumped to large amplitudes by the modulational instability where they then regulate the turbulent amplitude by shearing. A simple predator-prey model in which the turbulent amplitude ϕ drives a secondary instability V that is capable of turning off the transport was introduced in [107] (using slightly-different notation):

$$d\langle\phi^2\rangle/dt = \gamma\langle\phi^2\rangle - \alpha\langle\phi^2\rangle\langle V^2\rangle - \nu'\langle\phi^2\rangle^2 \quad d\langle V^2\rangle/dt = \alpha\langle\phi^2\rangle\langle V^2\rangle - \nu\langle V^2\rangle \quad (51)$$

where $\langle X \rangle$ is the ensemble average of X . Here, γ is the growth rate and ν' is the nonlinear damping rate of the drift-wave ϕ , and ν is the linear damping rate of the zonal flow V . This model conserves the energy between the shearing apart of drift waves and the pumping of the zonal flows, exchanged at rate α . The model clearly has a stationary state at the point where there is no flow $\langle V^2 \rangle = 0$ and the turbulence amplitude is set by nonlinear damping: $\langle\phi^2\rangle = \gamma/\nu'$. There is also an equilibrium with both flow and turbulence. For relatively weak nonlinear damping $\nu\nu' < \alpha^2$, the dynamic equilibrium is $\langle\phi^2\rangle \simeq \nu/\alpha$ and $\langle V^2\rangle \simeq \gamma/\alpha$. This simple model yields the important conclusion that the turbulent flux increases strongly with the zonal flow damping rate; if $\arg n_e/\phi = \delta$ then $D_{turb} \propto \langle\phi\rangle^2 \sin \delta = (\nu/\alpha) \sin \delta$. Thus, an increase in the damping of zonal flows could cause an increase in anomalous diffusivity. An order unity increase in damping would be of the correct order of magnitude to explain the observations.

7 Conclusion

In conclusion, the physics of ELM control using magnetic perturbations involves a rich interplay of various physical processes that possess nontrivial variation with plasma parameters. Two important physics issues appear to be resolved: (i) The dependence on β , shaping, and other aspects of the perturbation spectrum is likely to be due to resonant field amplification of the applied perturbations. (ii) A stochastic layer is not likely to form within the steep gradient region of the pedestal. The appearance of striated strike point patterns is not inconsistent with a perturbed layer outside of the steep-gradient region of the pedestal, but essentially no stochasticity inside of the steep-gradient region. However, a single island may form near the region where $\omega_e = \omega - \omega_{*e} \sim 0$, which typically occurs at the top of the pedestal, due to the steep gradient in electron temperature. The implications of this possibility are still under investigation because theoretical models that incorporate finite Larmor radius effects are required when the perturbation frequency is on the order of the drift frequency and/or when the size of the non-ideal region approaches the ion gyroradius. The dependence on collisionality is likely to be due to the mechanism for enhanced transport.

This article assessed three broad hypotheses for enhancing transport with non-axisymmetric magnetic fields: (i) enhanced transport due to an island or stochastic layer, (ii) enhanced axisymmetric neoclassical transport due to the change in ambipolar electric field, and (iii) interactions with turbulence. For small islands, outward transport due to either magnetic flutter fluxes or radiation of drift waves requires a zone of rotation where ions and electrons rotate in opposite directions relative to the perturbation $\omega_e\omega_i = (\omega - \omega_{*e})(\omega - \omega_{*i}) < 0$. The opposite condition yields enhanced confinement and differences in the pedestal rotation profile may explain the difference between high and low-collisionality ELM suppression results. All of the proposed mechanisms may be active simultaneously or yet another process may be responsible. The identification and determination of the process that dominates over a given span of collisionality is necessary for extrapolation to future devices.

Acknowledgements The author gratefully acknowledges fruitful collaborations and discussions with F. L. Waelbroeck and A. H. Boozer and would like to thank M. A. Dorf for a careful reading of the manuscript. The author would also like to thank the DIII-D team for the permission to analyze data for ELM suppression discharge 126006 and T. H. Osborne, in particular, for the use of his Python analysis tools. This work was performed under the auspices of the U.S. Department of Energy by Lawrence Livermore National Laboratory as LLNL-JRNL-512873 under Contract DE-AC52-07NA27344.

References

- [1] H. Zohm, Plasma Phys. Control. Fusion **38**, 105 (1996).

- [2] A. Loarte, G. Saibene, R. Sartori, et al., *Plasma Phys. Control. Fusion* **45**, 1549 (2003).
- [3] G. Federici, A. Loarte and G. Strohmayer, *Plasma Phys. Control. Fusion* **45** 1523 (2003).
- [4] J. Roth, E. Tsitrone, A. Loarte, et al., *J. Nucl. Mater.* **390**, 1 (2009).
- [5] T. E. Evans, R. A. Moyer, J. G. Watkins, et al., *Nucl. Fusion* **45**, 595 (2005).
- [6] K. H. Burrell, T. E. Evans, E. J. Doyle, et al., *Plasma Phys. Control. Fusion* **47**, B37 (2005).
- [7] T. E. Evans, R. A. Moyer, K. H. Burrell, et al., *Nature Phys.* **2**, 419 (2006).
- [8] T. E. Evans, M. E. Fenstermacher, R. A. Moyer, et al., *Nucl. Fusion* **48**, 024002 (2008).
- [9] T. E. Evans, R. A. Moyer, P. R. Thomas, et al., *Phys. Rev. Lett.* **92**, 235003 (2004).
- [10] W. Suttrop, T. Eich, J. C. Fuchs, et al., *Phys. Rev. Lett.* **106** 225004 (2011).
- [11] Y. Miura, M. Mori, T. Shoji, et al., *Fusion Sci. Tech.* **49**, 96 (2006).
- [12] J. M. Canik, R. Maingi, T. E. Evans, et al., *Phys. Rev. Lett.* **104**, 045001 (2010).
- [13] J. M. Canik, R. Maingi, T. E. Evans, et al., *Nucl. Fusion* **50**, 034012 (2010).
- [14] M. Bécoulet, E. Nardon, G. Huysmans, et al., *Nucl. Fusion* **48**, 024003 (2008).
- [15] M. J. Schaffer, J. E. Menard, M. P. Aldan, et al. *Nucl. Fusion* **48**, 024004 (2008).
- [16] Y. Liang, *Fusion Sci. Tech.* **59**, 586 (2011).
- [17] N. Oyama , P. Gohil , L. D. Horton et al., *Plasma Phys. Control. Fusion* **48** A171 (2006).
- [18] D. Whyte, A. E. Hubbard, J. W. Hughes, *Nucl. Fusion*, **50** 105005 (2010).
- [19] A. H. Boozer, *Phys. Plasmas* **16**, 052505 (2009).
- [20] J. D. Callen, C. C. Hegna, and A. J. Cole, *Phys. Plasmas* **17**, 056113 (2010).
- [21] M. E. Fenstermacher, T. E. Evans, T. H. Osborne, et al., *Phys. Plasmas* **15**, 056122 (2008).
- [22] R. Fitzpatrick, *Phys. Plasmas* **5**, 3325 (1998).
- [23] A. B. Rechester and M. N. Rosenbluth, *Phys. Rev. Lett.* **40**, 38 (1978).
- [24] J. C. Vallet, L. Poutchy, M. S. Mohamed-Benkadda, *Phys. Rev. Lett.* **67** 2662 (1991).
- [25] A. Grosman, J. M. Ané, et al., *J. Nucl. Mater.* **313** 1314 (2003).
- [26] I. Joseph, R. A. Moyer, T. E. Evans, et al., *J. Nucl. Mater.* **363**, 591 (2007).
- [27] I. Joseph, T. E. Evans, A. M. Runov, et al., *Nucl. Fusion* **48**, 045009 (2008).
- [28] H. Frerichs, D. Reiter, O. Schmitz, et al., *Nucl. Fusion* **50**, 034004 (2010).
- [29] G. Park, C. S. Chang, I. Joseph, and R. A. Moyer, *Phys. Plasmas* **17**, 102503 (2010).
- [30] M. F. Heyn, I. B. Ivanov, S. V. Kasilov, et al., *Nucl. Fusion* **48**, 024005 (2008).
- [31] V. A. Izzo and I. Joseph, *Nucl. Fusion* **48**, 115004 (2008).
- [32] H. R. Strauss, L. Sugiyama, G. Y. Park, et al, *Nucl. Fusion* **49**, 055025 (2009).
- [33] M. Bécoulet, G. Huysmans, X. Garbet, et al., *Nucl. Fusion* **49**, 085011 (2009).
- [34] E. Nardon, P. Tamain, M. Bécoulet, et al., *Nucl. Fusion* **50**, 034002 (2010).
- [35] F. L. Waelbroeck, I. Joseph, E. Nardon, et al, "Plasma response to resonant magnetic perturbations," submitted to *Nucl. Fusion* (2011).
- [36] M. Z. Tokar, T. R. Singh, and B. Unterberg, *Phys. Plasmas* **15**, 072515 (2008).
- [37] V. Rozhansky, E. Kaveeva, P. Molchanov, et al., *Nucl. Fusion* **50**, 034005 (2010).
- [38] V. Rozhansky, P. Molchanov, E. Kaveeva, et al., *Nucl. Fusion* **51**, 083009 (2011).
- [39] R. A. Moyer, T. E. Evans, T. H. Osborne, *Phys. Plasmas* **12**, 056119 (2005).
- [40] T. E. Evans, K. H. Burrell, M. E. Fenstermacher, et al., *Phys. Plasmas* **13**, 056121 (2006).
- [41] H. R. Wilson et al., *Phys. Plasmas* **9**, 1277 (2002).
- [42] P. B. Snyder, et al., *Phys. Plasmas* **9**, 2037 (2002).
- [43] T. E. Evans, R. K. W. Roeder, J. A. Carter, et al., *J. Phys.: Conf. Ser.* **7**, 174 (2005).
- [44] T. E. Evans, I. Joseph, R. A. Moyer, *J. Nucl. Mater.* **363** 570 (2007).
- [45] R. A. Moyer, K. H. Burrell, T. E. Evans, Proc. 21st IAEA Fusion Energy Conference (2006), paper EX/9-3.
- [46] J. G. Watkins, T. E. Evans, M. W. Jakubowski, *J. Nucl. Mater.* **390-391**, 839 (2009).
- [47] Y. Liang, H. R. Koslowski, P. R. Thomas, et al., *Phys. Rev. Lett.* **98**, 265004 (2007).
- [48] A. Kirk, Yueqiang Liu, E. Nardon, et al., *Plasma Phys. Control. Fusion* **53**, 065011 (2011).
- [49] T. H. Osborne, P. B. Snyder, K. H. Burrell, et. al, *J. Phys.: Conf. Ser.* **123**, 012014 (2008).
- [50] O. Schmitz, T. E. Evans, M. E. Fenstermacher, et al., *Plasma Phys. Control. Fusion* **50**, 124029 (2008)
- [51] M. W. Jakubowski, T. E. Evans, M. E. Fenstermacher, et al., *Nucl. Fusion* **49**, 095013 (2009).
- [52] A. Kirk, E. Nardon, R. Akers, et al., *Nucl. Fusion* **50**, 034008 (2010).
- [53] E. Nardon, A. Kirk, R. Akers, et al., *Plasma Phys. Control. Fusion* **51**, 124010 (2009).
- [54] J.-W. Ahn, J. M. Canik, V. A. Soukhanovskii, et al., *Nucl. Fusion* **50**, 045010 (2010).
- [55] J.-W. Ahn, R. Maingi, J. M. Canik, et al., *Phys. Plasmas* **18**, 056108 (2011).
- [56] A. H. Boozer, *Phys. Plasmas* **3** 4620 (1996).
- [57] A. H. Boozer, *Phys. Rev. Lett.* **86**, 5059 (2001).
- [58] H. Reimerdes, J. Bialek, M. S. Chance, et al., *Nucl. Fusion* **45**, 368 (2005).
- [59] M. P. Gryaznevich, T. C. Hender, D. F. Howell, et al., *Plasma Phys. Controlled Fusion* **50**, 124030 (2008).
- [60] C. Nuhrenberg and A. H. Boozer, *Phys. Plasmas* **10** 2840 (2003).
- [61] A. H. Boozer and C. Nuhrenberg, *Phys. Plasmas* **13** 102501 (2006).
- [62] J.-K. Park, A. H. Boozer, and A. H. Glasser, *Phys. Plasmas* **14**, 052110 (2007).

- [63] A. H. Glasser and M. S. Chance, Bull. Am. Phys. Soc. **42**, 1848 (1997), abstract dMopP12.
- [64] J.-K. Park, M. J. Schaffer, J. E. Menard and A. H. Boozer, Phys. Rev. Lett. **99**, 195003 (2007).
- [65] Y.-Q. Liu, A. Kirk, and E. Nardon Phys. Plasmas **17**, 122502 (2010).
- [66] Y.-Q. Liu, A. Kirk, and Y. Gribov, et al., Nucl. Fusion **51**, 083002 (2011).
- [67] R. D. Hazeltine and J. D. Meiss, Phys. Rep. **121**, 1 (1985).
- [68] F. L. Waelbroeck, Nucl. Fusion **49**, 104025 (2009).
- [69] F. L. Waelbroeck, Phys. Plasmas **10**, 4040 (2003).
- [70] A. Cole and R. Fitzpatrick, Phys. Plasmas **13**, 032503 (2006).
- [71] R. Fitzpatrick and F. L. Waelbroeck, Phys. Plasmas **16**, 072507 (2009).
- [72] R. Fitzpatrick and F. L. Waelbroeck, Phys. Plasmas **17**, 062503 (2010).
- [73] R. Fitzpatrick and F. L. Waelbroeck, Plasma Phys. Control. Fusion **52**, 055006 (2010).
- [74] P. H. Rutherford, Phys. Fluids **16**, 1903 (1973).
- [75] J. F. Drake and Y. C. Lee, Phys. Fluids **20**, 1341 (1977).
- [76] A. I. Smolyakov, Plasma Phys. Control. Fusion **35**, (1993) 657.
- [77] R. Fitzpatrick, Nucl. Fusion **33**, 1049 (1993).
- [78] R. Fitzpatrick, Phys. Plasmas **2**, 825 (1995).
- [79] C. C. Hegna, Phys. Plasmas **6**, 1767 (1998).
- [80] H. R. Wilson, Trans. Fusion Sci. Tech. **57**, 164 (2010).
- [81] Q. Yu and S. Günter Nucl. Fusion **49**, 062001 (2009).
- [82] Q. Yu and S. Günter Nucl. Fusion **51**, 073030 (2010).
- [83] M. F. Heyn, I. B. Ivanov, S. V. Kasilov, and W. Kernbichler, Nucl. Fusion **46** S159 (2006).
- [84] K. C. Shaing, Nucl. Fusion **50** 025022 (2010).
- [85] J.-K. Park, Phys. Rev. Lett. **102**, 065002 (2009).
- [86] K. C. Shaing, Phys. Plasmas **9** 3470 (2002).
- [87] K. C. Shaing, Nucl. Fusion **43** 253 (2003).
- [88] S. P. Hirshman and D. J. Sigmar, Nucl. Fusion **21**, 1079 (1981).
- [89] F. L. Hinton and R. D. Hazeltine, Rev. Mod. Phys. **48**, 239 (1976).
- [90] T. D. Rognlien and D. D. Ryutov, Contrib. Plasma Phys. **38**, 152 (1998).
- [91] V. Rozhansky, E. Kaveeva, and S. Voskoboinikov, et. al, Phys. Plasmas **9**, 3385 (2002).
- [92] L. M. Kovrizhnikh, Sov. Phys. JETP **29**, 475 (1969).
- [93] M. N. Rosenbluth, P. H. Rutherford, J. B. Taylor, E. A. Frieman, and L. M. Kovrizhnikh, Proc. Fourth Int. Conf. on Plasma Phys. and Control. Nucl. Fusion Research, Madison, WI, 17-23 June, 1971 (International Atomic Energy Agency, Vienna, 1971), Vol. I, p. 495, Paper No. IAEA-CN-28/C-12.
- [94] Yueqiang Liu, M. S. Chu, I. T. Chapman and T. C. Hender, Phys. Plasmas **15** 112503 (2008).
- [95] A. Cole and R. Fitzpatrick, Phys. Plasmas **18**, 055711 (2011).
- [96] M. N. Rosenbluth, R. Z. Sagdeev, J. B. Taylor and G. M. Zaslavski, Nucl. Fusion **6** 297 (1966).
- [97] R. W. Harvey, M. G. McCoy, J. Y. Hsu and A. A. Mirin, Phys. Rev. Lett. **47** 102 (1981).
- [98] I. Kaganovich and V. Rozhansky, Phys. Plasmas **5**, 3901 (1998).
- [99] A. M. Runov, D. Reiter, S. V. Kasilov, et al., Phys. Plasmas **8**, 916 (2001).
- [100] H. R. Wilson and J. W. Connor, Plasma Phys. Control. Fusion **51**, 115007 (2009).
- [101] F. L. Waelbroeck, J. W. Connor, and H. R. Wilson, Phys. Rev. Lett. **87**, 215003 (2001).
- [102] R. Fitzpatrick and F. L. Waelbroeck, Phys. Plasmas **12**, 122511 (2005).
- [103] F. Militello and F. L. Waelbroeck, Nucl. Fusion **49** 065018 (2009).
- [104] M. Leconte, P. Beyer, X. Garbet, and S. Benkadda, Phys. Rev. Lett. **102**, 045006 (2009)
- [105] M. Leconte, P. Beyer, X. Garbet, and S. Benkadda, Nucl. Fusion **50** (2010) 054008
- [106] P. Beyer, F. de Solminihac, M. Leconte, et al., Plasma Phys. Control. Fusion **53**, 054003 (2011).
- [107] P. H. Diamond, S.-I. Itoh, K. Itoh and T. S. Hahm, Plasma Phys. Control. Fusion **47**, R35 (2005).
- [108] A. Zagorodny and J. Weiland, Phys. Plasmas **6**, 2359 (1999).